Doctoral Dissertation

Doctoral Program in Materials Science and Technology (36rd Cycle)

# Investigating the Effects of Hot Isostatic Pressing on Additively Manufactured parts

By

**Hanieh Bakhshi Farkoush**

*******

**Supervisor(s):**
Prof. S. Biamino, Supervisor
Dr. G. Marchese, Co-Supervisor

**Doctoral Examination Committee:**
Prof. D. Milanese, Referee, University of Parma
Prof. F. Sarasini, Referee, Sapienza University of Rome

Politecnico di Torino 2024

May 12, 2024

I hereby declare that, the contents and organisation of this dissertation constitute my own original work and does not compromise in any way the rights of third parties, including those relating to the security of personal data.

…….....

Hanieh Bakhshi Farkoush

Turin, March 04, 2024

# Summary

This thesis delves into the transformative effects of Hot Isostatic Pressing (HIP) on components fabricated through Additive Manufacturing (AM) methods, focusing on the Electron Beam Powder Bed Fusion (EB-PBF) and Laser Powder Bed Fusion (L-PBF) of Ti6Al4V and TiAl alloys. The research is pivotal for the aerospace and biomedical sectors, where the mechanical integrity and performance of materials are paramount. It aims to refine AM processes to overcome prevalent challenges such as porosity, deformation, and inconsistent microstructures, thereby elevating the mechanical properties and reliability of produced parts.

The investigative journey begins with an in-depth exploration of EB-PBF and L-PBF techniques, spotlighting their potential and limitations in processing Ti6Al4V and TiAl alloys. The study meticulously examines the microstructural evolution influenced by varying HIP conditions, providing a nuanced understanding of how HIP treatment can significantly mitigate defects and enhance material characteristics. For TiAl alloys, a critical breakthrough was achieved by identifying optimal EB-PBF process parameters that crucially reduce aluminum evaporation— a significant hurdle that impacts microstructural uniformity and mechanical strength. This optimization ensures the production of denser components with a more uniform microstructure, tailored for high-temperature applications.

Parallelly, the thesis's exploration into Ti6Al4V alloy unveils how HIP effectively diminishes porosity, fostering an improvement in overall material quality. A predictive model emerges from this analysis, offering a strategic guide to optimize LPBF process parameters and HIP conditions. This model stands as a cornerstone for manufacturing near-full density Ti6Al4V components, adeptly managing deformation to maintain structural integrity, especially in encapsulated materials tailored for specific applications.

In conclusion, this thesis significantly advances the AM field, elucidating the intricate relationship between AM process parameters, HIP treatments, and the resulting material properties. The findings not only propel the current understanding of Ti6Al4V and TiAl alloys forward but also lay a solid groundwork for future endeavors aiming to refine AM techniques and post-processing treatments. As we edge into a new era of materials engineering, this work

highlights the critical importance of ongoing exploration and innovation in AM, heralding a future where the potential of material performance continues to expand.

By bridging gaps in current knowledge and introducing novel methodologies, this research marks a pivotal step towards the realization of more efficient, sustainable, and higher quality manufacturing practices. The journey of discovery in the realms of additive manufacturing and HIP processing is far from concluded, with each new insight pushing the boundaries of what is possible in material science and engineering.

# Acknowledgment

The path to completing this doctoral program has been a journey of academic and personal growth, made possible by the support and guidance of many. I am deeply grateful for the opportunity to acknowledge those who have played a pivotal role in my research and development.

Foremost, I extend my sincerest gratitude to my supervisors, Prof.Sara Biamino and Dr.Giulio Marchese, whose expertise, patience, and insightful feedback have been invaluable throughout this journey. Your guidance has not only shaped this research but has also significantly contributed to my personal and professional development.

I am equally thankful to my host supervisor at the University of Twente, Dr. Davoud Jafary, for welcoming me into the academic community and providing the resources and environment conducive to my research. Your support has been crucial in navigating the complexities of my doctoral work.

Special appreciation goes to my mentor, Ian Gibson. Your mentorship and the wealth of knowledge you shared have been instrumental in refining jurney. Your encouragement and belief in my capabilities have been a constant source of motivation.

I am also grateful to the entire team at the University of Twente, DMP department, and Fraunhofer Innovation platform for their collaboration, insights, and the stimulating academic environment they provided. Working alongside such dedicated professionals has been both an honor and a privilege.

To my family and friends, who have provided unwavering support and encouragement throughout this journey, your belief in me has been a cornerstone of my perseverance and success. I cannot thank you enough for your love and understanding during this challenging yet rewarding process.

This accomplishment reflects not only my efforts but the collective support and encouragement of each individual mentioned and many others who have contributed in various capacities. I am profoundly thankful for your contributions to my doctoral journey

# *Dedication*

*To my father, my wellspring of strength, ambition, and determination. You taught me the art of perseverance, revealing that dreams know no bounds and illustrating how to reach them by tapping into my own potential. Simply witnessing your resolve was enough to fuel my ambition and lift my spirits towards greater heights. I am truly blessed to call you my father, mentor, and best friend. You anchor me to my true self in moments of doubt and are my steadfast believer when uncertainty clouds my vision.*

*To my mother, who unveiled the beauty of continuous learning and personal growth. Your unconditional love and support have been my warmth in the coldest times. Your wisdom lights my way, and your sacrifices do not go unnoticed. You've shown me that every challenge is an opportunity for growth and that kindness and grace are among our greatest strengths.*

*To my dearest sister and brother, you are my enduring source of hope and strength. Your aspirations and achievements inspire me deeply, and I am committed to making your path smoother. Celebrating your successes provides me with endless motivation and joy. Your unwavering support and belief in me have been fundamental throughout this journey.*

*And to Fabrizio, the love of my life, my journey would be incomplete without you. My co-conspirator in life's grand adventure, you've stood by my side through our darkest days, fighting every battle with unwavering support. Together, we have overcome and will continue to conquer, side by side, as we step into the dawn of our shared dreams. This is only the beginning of our story.*

*Special thanks to Dr Amirreza Alavi, Marshall Bruce Mathers III, Farrokh Bulsara, Jim Parsons, Ali Bandari, Dr. Azarakhsh Mokri, and Heli Hendesi for always being there for me.*

# Contents

# List of Tables

# List of Figures

# Chapter 1

# State of Art

## 1.1 Additive Manufacturing (AM)

Additive Manufacturing (AM) technologies have revolutionized the production of components, offering unparalleled design flexibility [1][2]. The beauty of AM lies in its ability to create complex shapes that were once deemed impossible using conventional methods. By employing AM, we embrace a near-net shape approach, bypassing the need for time-consuming machining and joining processes. This not only expedites production but also reduces material wastage, making AM a sustainable choice [3] .

As shown in Figure 1, although AM can involve greater initial expenditures in contrast to conventional methods, its notable cost reductions stem from the cost reduction for the production of complex shape components. This, in turn, renders the ultimate component price more competitive. Consequently, the benefits of AM technology extend beyond the upfront expenses, encompassing both the intricacy of the final component and the broader manufacturing economics [4][5][6]. Moreover, AM offers financial advantages by proving cost-effective for producing intricately designed, low-volume components compared to traditional methods, yet its cost-effectiveness diminishes for high-volume production, where conventional manufacturing methods often retain their economic edge. For instance, in the biomedical field, AM allows for the creation of intricately designed, patient-specific orthopedic implants that enhance comfort and healing, while in aerospace, it facilitates the production of lightweight components like aircraft brackets, contributing to reduced fuel consumption and operational costs.

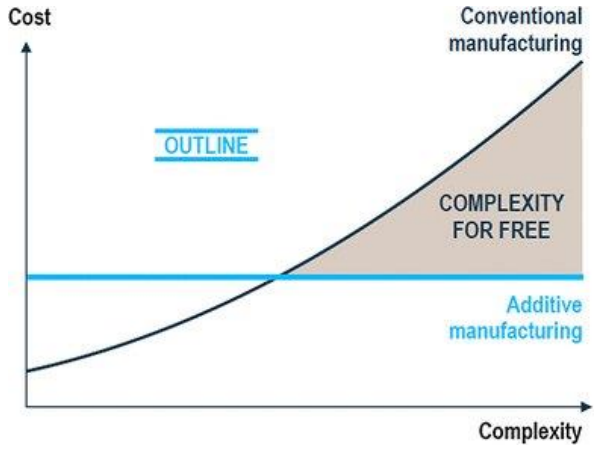


**Figure 1: Cost vs. complexity between AM and conventional manufacturing methods [2]**

AM originally found its foothold in the industrial landscape through its application in prototyping. In the 1980s, this technology was known as Rapid Prototyping (RP), and it offered engineers a game-changing approach to create prototypes directly from computer-aided design (CAD) models, bypassing the need for cumbersome tooling operations. The versatility of AM allowed for the swift production of complex shapes, making it a valuable asset for engineers seeking efficient and rapid prototyping solutions, as shown in Figure 2 [7].

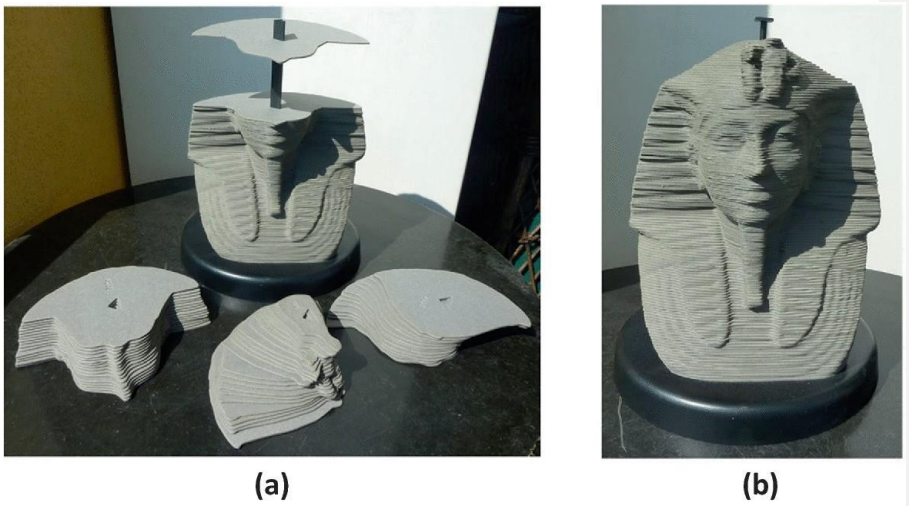


**Figure 2: General additive manufacturing principle: a layer buildup, b finished product [8]**

Over time, the scope of AM has expanded dramatically, and it has transitioned from merely prototyping to becoming a viable method for manufacturing final functional products in small to medium quantities [9]. This shift has revolutionized traditional manufacturing processes, enabling the fabrication of end-user products with unparalleled complexity and design flexibility. AM has emerged as a transformative technology, opening new possibilities for cost-effective and customized production in various industries, as illustrated in Figure 3 [9].

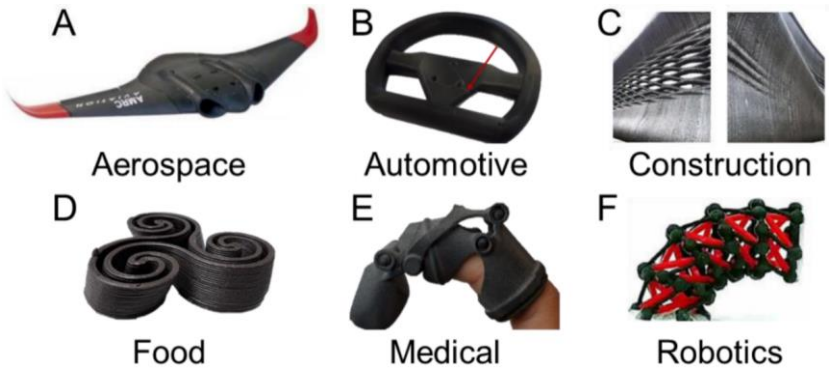


**Figure 3: Representative innovative AM applications in diverse fields demonstrating (A) an unmanned aerial vehicle, (B) a lightweight steering wheel, (C) bridge construction, (D) a chocolate printed geometry, (E) a finger prosthetic], and (F) a soft tensegrity robot. Images adapted with permission.[10]**

### 1.1.1 Industrial Applications of AM:

In recent years, AM has witnessed widespread adoption across various industrial sectors, including the automotive and aerospace industries, marking a transformative shift in manufacturing processes [11][5][12]. The automotive sector, in particular, has eagerly embraced AM, employing it for rapid prototyping, tooling, and component production, thereby realizing a spectrum of advantages ranging from design improvements to cost efficiencies and enhancements in vehicle performance [13]. The deployment of AM in rapid prototyping expedites iterative design processes, yielding notable reductions in both development time and costs. Beyond this, AM's unique capability to fabricate intricate geometries, often unattainable through conventional manufacturing methods, has fueled innovation, leading to the emergence of optimized structural designs and reduced component weight. This multifaceted enhancement not only augments vehicle efficiency but also contributes to advancements in fuel economy and the reduction of emissions. Moreover, AM facilitates on-demand custom tooling and fixture production within the automotive sector, streamlining manufacturing processes and enhancing cost-effectiveness as shown in Figure 4. In the medical domain, AM has proven revolutionary, particularly in patient-specific implant and prosthetic production, ensuring superior fit and functionality while simultaneously minimizing complications and post-operative discomfort [14]. As shown in Figure 5, the utilization of medical models created

through AM has provided invaluable support to surgeons in the visualization and planning of intricate medical procedures, thereby elevating precision and success rates. Furthermore, AM's intrinsic flexibility, which extends to both design and material selection, has paved the way for biocompatible implants that closely mimic the mechanical properties of human tissues, as shown in Figure 6. This innovation opens doors to the creation of high-performance implants that seamlessly integrate with the human body, thereby mitigating the risk of rejection and optimizing long-term patient outcomes [11][5][12].

**Figure 4: Assembly of machined SEB-PBF turbocharger wheel and shaft. Machining was realized for double hexagon head, radius of turbine blades as well as back face. The assembling between shaft and turbocharger wheel was performed by brazing[13]**

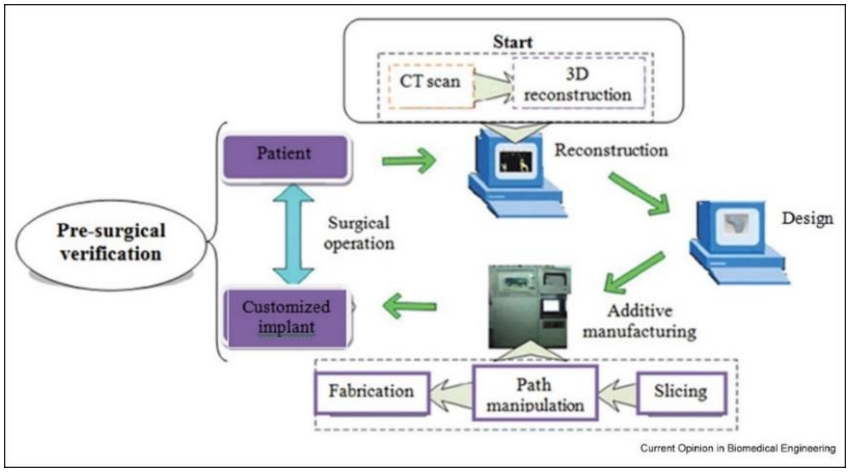


**Figure 5: Schematic of AM of customized biomedical part[5]**

**Figure 6: Schematic diagram of the biomedical application of additive manufacturing of bio metals includes cranial prosthesis, dental implants, acetabular cup, interbody fusion cage, hip prosthesis and knee prosthesis. [12]**

In the aerospace industry, AM has introduced groundbreaking changes through its layer-by-layer manufacturing approach, utilizing common feedstock and digitally defined heat source trajectories. This transformative approach has revolutionized production, enabling the fabrication of intricate and lightweight components, consequently shortening lead times and fostering advancements across various aerospace sectors as shown in Figure 7 and in references [15][2]. For high-volume production scenarios, traditional manufacturing methods often retain a cost advantage, necessitating a judicious assessment of the commercial viability of AM. The enthusiastic adoption of AM in both the automotive and aerospace industries has unlocked new vistas of customized production, efficiency enhancements, and innovative design solutions. The transformative potential of AM transcends mere advancements in manufacturing, as it plays a pivotal role in shaping the future landscape of healthcare innovation. These developments underscore the multifaceted implications of AM across diverse industries, casting a profound impact on manufacturing processes and paving the way for revolutionary healthcare innovations [16][17].

**Figure 7: TO and AM of Airbus A320 nacelle hinge bracket. Left: TO design process. Right: Original bracket (top) and final TO optimized design (bottom). Original steel bracket = 918 g; TO and AM bracket in Ti6Al4V = 326 g. Copyright: Airbus[17]**

### 1.1.2 Classification of AM

The classification of AM forms a fundamental framework for comprehending its diverse technologies and applications. AM encompasses eight primary categories, as shown in Figure 8. Powder bed fusion involves selectively fusing a fine powder with laser or electron beams. Material jetting and binder jetting entail the jetting of material droplets or binder agents onto a build platform. Sheet lamination bonds sheets of material to form objects, and directed energy deposition melts and fuses materials using focused energy sources. This systematic classification underpins the study and application of AM across diverse industries. It is imperative to delve into the materials used In AM, particularly polymers and metals, for their pivotal roles in shaping the technology's capabilities and applications. Polymers, offering versatility, ease of processing, and diverse options, find use in various sectors, from prototyping to aerospace. Metals, renowned for strength and durability, feature prominently in industries such as aerospace and automotive.

This discussion focuses on two key metal AM processes: Laser Powder Bed Fusion (L-PBF), and Electron Beam Powder Bed Fusion (EB-PBF), known for their precision and capacity to produce structurally robust, complex metal components, exemplifying advanced manufacturing techniques [14][18].

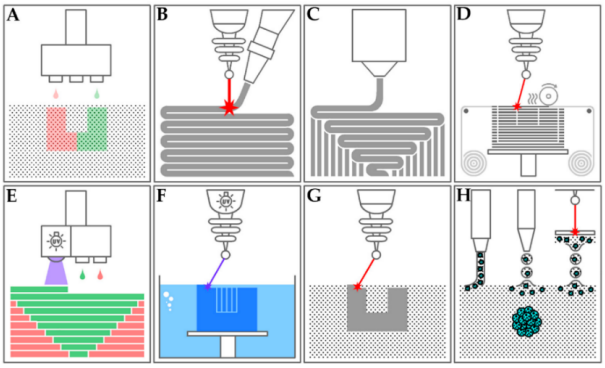


**Figure 8: Types of additive manufacturing (AM). (A) Binder jetting. (B) Directed energy deposition (C) Material extrusion (D) Sheet lamination (E) Material jetting (MJ (F) Stereolithography (G) Powder bed fusion (H) Extrusion bioprinting. All figures are designed and created by the authors[14]**

## 1.2 Powder Bed Fusion (PBF) Techniques

PBF techniques have ushered in a transformative era within AM, facilitating the fabrication of intricate and functional three-dimensional objects. The origins of PBF trace back to the 1980s [19]. PBF, a leading AM technique, begins by evenly distributing a thin layer of powdered material, typically metals or alloys, across a build platform. A high-energy source, frequently a laser or electron beam, meticulously scans the designated areas, melting and solidifying the powder layers, adhering to a digital design model. PBF distinguishes itself with unparalleled accuracy, enabling the fabrication of intricate and structurally sound components[9][20]. Its versatility finds applications in aerospace and healthcare, where precision and customization are paramount. This scientific rigor and precision make PBF an indispensable tool in advanced manufacturing, ensuring the production of components meeting rigorous engineering specifications [9][20][21]. EB-PBF and L-PBF, as two branches of PBF, will be discussed in detail in the subsequent section, highlighting their significance in AM for advanced industrial applications.

### 1.2.1 EB-PBF

Electron beam powder bed fusion (EB-PBF) utilizes an electron beam as a heat source to melt the feedstock powder material in a powder-bed configuration [42]. EB-PBF, a versatile technique, exhibits a notable array of advantageous component characteristics. This encompasses characteristics like low residual stress and minimal contamination. These attributes are owed to a meticulously engineered machine design [22]. It operates by consistently maintaining the material at elevated temperatures during the entire manufacturing procedure, all conducted within a vacuum-sealed build chamber [23]. This well-considered

operational environment profoundly contributes to the exceptional quality and reliability of the manufactured components [24][25].

In the context of EB-PBF, the process operates under vacuum conditions ranging from 10^-4 to 10^-5 mbar, a crucial consideration for metals and alloys prone to gas affinity. In the case of the ARCAM machines, a controlled vacuum environment, maintained with a slight helium pressure of 10^-3 mbar, prevents electrostatic charging and smoke events that could disrupt the process. Electrons emitted by a tungsten filament or a lanthanum hexaboride (LaB6) cathode are accelerated to 60 kV and controlled with electromagnetic lenses, as shown in Figure 9. With beam currents between 1 and 50mA, maximum beam power reaches about 3kW. [26]. Notably, the LaB6 cathode offers stability for beam production at higher powers, while being sensitive to smoke events, suitable primarily for processing titanium. Powder layer thickness aligns with intended layer thickness, typically ranging from 50 µm to 150 µm. After reaching a determined temperature on the start plate by defocusing the electron beam on the start plate, the process begins with applying the first layer of powder , often stainless steel, with a temperature just above the building temperature. Matching or resembling plate and building materials minimizes contamination, especially for high-performance materials [27][28][29].

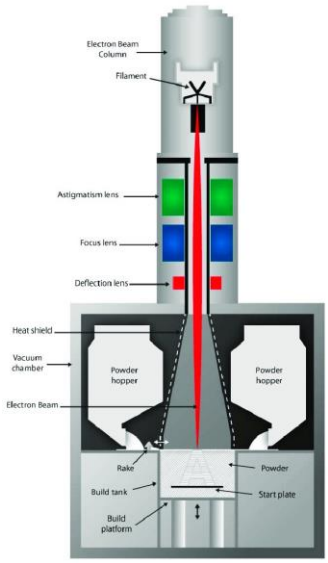


**Figure 9: Schematic of the electron beam melting (EB-PBF) process [25]**

The process chamber and the steps of production are displayed in Figure 10. The cycle initiates with the distribution of powder above the starting plate, which is followed by the pre-

heating of the powder layer using an electron beam, as indicated by "heating" in Figure 10: EB-PBF process. Left: Process chamber. Right: 4-step process for building one layer[27].

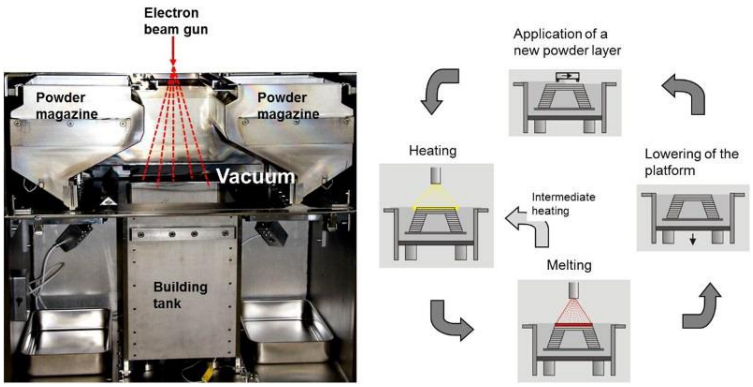


**Figure 10: EB-PBF process. Left: Process chamber. Right: 4-step process for building one layer[27]**

In the preheating phase, the electron beam undergoes defocused scanning across the powder layer, serving a dual purpose: maintaining the temperature within the building volume and promoting the sintering of powder particles. This sintering step is crucial for enhancing the electrical conductivity of the powder and preventing potential process instabilities like the well-known 'smoke' phenomenon, which occurs when charged powder particles repel each other, leading to machine disruption. The specific preheating temperature and strategy depend not only on the particular metal or alloy being used but also on the properties of the powder itself. Generally, the temperature is determined under the starting plate, and ranges from approximately 400°C to 1100°C, varying with the material. The intricate balance among sintering, alloy composition, and oxide layer constitution guides temperature choices [30][31].

As shown in Figure 11a, after the preheating phase, the subsequent step entails precisely scanning the electron beam over the powdered layer, usually at a reduced velocity. This controlled scanning process selectively melts the powder particles at specific locations where solid material is intended to take shape. It is worth noting that this melting process discriminates between different areas and contours within the build[26][29][32]. Numerous crucial process parameters require meticulous definition, including beam power (P), beam velocity (v), the distance between scanning lines known as line offset (d), focus offset of the beam, the number of contours, and several others [33]. The process of selectively melting areas is typically accomplished using a hatching pattern, wherein the orientation of the electron beam shifts by 90° in each successive line and layer, as illustrated in Figure 11-b. Additionally, EB-PBF introduces the capability of melting contours through what is referred to as the quasi-multi-beam mode (Figure 11-c). In this mode, quasi-simultaneous melting of contours at multiple points, sometimes up to 100, is achieved through point-to-point beam jumping. This strategic approach is employed to improve surface quality and reduce roughness in the manufactured components [28][27].

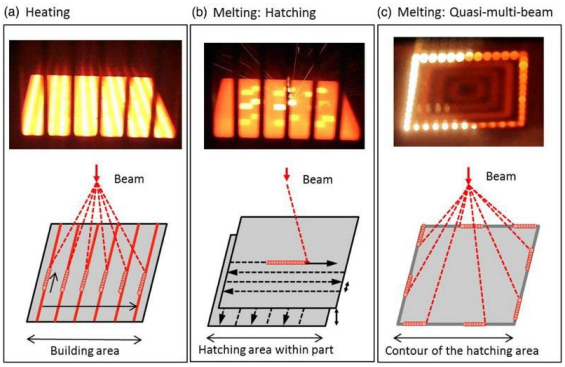


**Figure 11: Heating and melting during EB-PBF. At the top: photograph during the process. At the bottom: schematic of the beam movement. a Heating by quasi-multi-beam scanning of the total building area with a defocused beam, b Melting by hatching, c Quasi-multi-beam contour melting by jumping from point to point [27].**

What gives EB-PBF a distinct advantage in AM technologies are the unique benefits derived from its utilization of an electron beam in a vacuumed chamber with preheating steps. Elevated building temperatures have a substantial impact on the microstructure and residual stresses. In comparison to laser-based AM processes, EB-PBF demonstrates lower levels of residual stress and coarser microstructures due to altered cooling rates and temperature gradients. This unique thermal environment results in the components being embedded within a partially sintered powder bed upon completion of the build. To facilitate powder removal and separation, sandblasting with the same powder particles as abrasive is employed [26].

In the context of EB-PBF, Area Energy (AE) plays a crucial role in understanding the densification process within the alloy as well as the final microstructure. AE serves as a fundamental metric to assess energy distribution and absorption dynamics during melting and solidification, providing valuable insights into the interplay between energy input, material properties, and microstructural evolution. By incorporating AE analysis, researchers can optimize processing parameters, enhancing component quality and performance. AE quantifies the energy input per unit area during the melting and solidification stages, directly impacting temperature distribution, phase changes, and microstructural evolution. Monitoring and analyzing AE offer insights into heat transfer mechanisms, enabling process control strategies for achieving desired microstructure, mechanical properties, and dimensional accuracy. The formula for AE calculation involves integrating parameters related to energy input and surface area, typically expressed as joules per square millimeter ($J/mm^2$). This quantification aids in understanding thermal dynamics, heat distribution, and material behavior during manufacturing, facilitating informed decisions for optimizing process parameters and ensuring structural integrity [34][35].

### 1.2.2 L-PBF

The core concept behind L-PBF in AM is to melt and fuse materials layer by layer using a laser as the heat source. In the context of metal AM, L-PBF is a crucial technique, but it can be affected by various factors before building parts. Over many decades, numerous studies have been conducted to explore how choices in process parameters, such as laser power and layer thickness, impact different materials. These studies aim to make the L-PBF process work as effectively as possible for each material, highlighting the importance of L-PBF in the world of additive manufacturing [19]. As a result, this technology has become a highly sought-after method for the production of high-performance components in numerous industries [22].

L-PBF technology is also known as Selective Laser Melting (SLM) and Direct Metal Laser Sintering (DMLS). These terminologies are commonly used interchangeably to denote the process whereby powdered materials are fused and solidified using a high-powered laser to fabricate intricate three-dimensional structures layer by layer. L-PBF, SLM, and DMLS share fundamental procedural similarities, underscoring the widespread applicability and versatile nature of this AM approach across diverse industrial domains. In the realm of metal AM, L-PBF has emerged as a focal point of research and development. L-PBF entails meticulous control of essential process parameters, as shown in Figure 12, such as laser power, scan speed, layer thickness, and hatching distance, each crucial for achieving precise energy levels during the fabrication of various metallic materials. Furthermore, this technology has spurred extensive investigations into the mechanical properties of L-PBF-produced components, the influence of orientation, build layout, scanning strategies on part performance, and the common challenges and defects encountered throughout the L-PBF process.

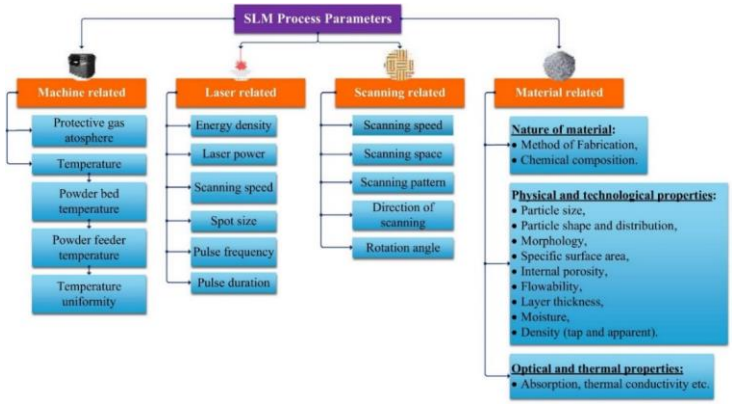


**Figure 12: Major L-PBF process parameters[36]**

Figure 13 shows that the L-PBF production process involves a series of well-coordinated steps that form the basis for crafting intricate and functional components [36]. Beginning with the extraction of design data from three-dimensional CAD/STL files, these files undergo a digital transformation and are divided into thin geometric layers[27]. As shown in Figure 14, using a high-energy laser, powdered material undergoes controlled fusion, layer by layer, while the build platform progressively moves downward along the Z-axis. The initial layers of powdered material are carefully fused onto a level base, paving the way for successive layers of powder to be added meticulously on top of the solidified foundations. This process culminates in the creation of the final component. L-PBF's utilization of a powerful laser directly melts powder particles into a molten state, resulting in near-dense parts that reduce the need for extensive post-treatments [37][38].

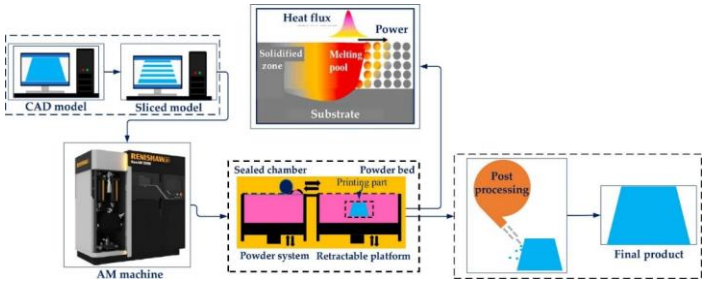


**Figure 13: Working principle of L-PBF process [36]**

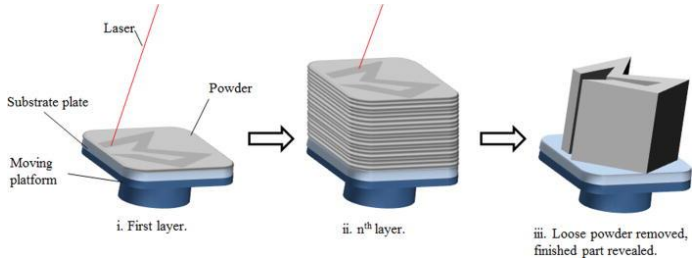


**Figure 14: Concept of L-PBF process. (i) High-power laser melts selective areas of the powder bed. (ii) Process is repeats for successive layers. (iii) Loose powder removed and finished part revealed [38]**

The scanning strategy in L-PBF is a crucial aspect that governs the path of the laser beam as it interacts with the powder bed. It involves determining the sequence and pattern of the laser scans across each layer, as shown in Figure 15. The choice of scanning strategy impacts factors like heat distribution, cooling rates, and the overall mechanical properties of the final part. By selecting an appropriate scanning strategy, manufacturers can optimize the quality of the parts, minimize distortion, and effectively manage thermal effects during the L-PBF process [39][40].

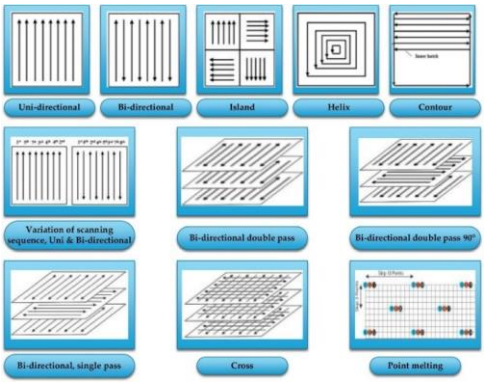


**Figure 15: Common types of scanning strategies[36]**

The concept of "Volumetric Energy Density (VED)" holds paramount importance in the domain of melting powder materials for manufacturing purposes. This metric signifies the energy from the laser beam that impacts a specific volume of powder material and has a connection with various laser and scan parameters. As shown in Figure 17, VED is essentially comprised of four controllable process factors: (1) laser power (W), which represents the energy intensity of the laser beam; (2) scanning speed (mm/s), indicating the speed of the laser beam's movement; (3) hatch distance (mm), referring to the gap between two adjacent scan paths; and (4) layer thickness (mm), denoting the thickness of a single layer of the powder bed, equivalent to one incremental amount of the powder bed. Utilizing the same energy density value with different parameters in the L-PBF process leads to distinct material characteristics. Furthermore, the specific value of energy density varies among different materials, and exceeding a material's energy density range results in a broader and deeper melt pool. The empirical formula for VED is derived as follows:

$$VED = \frac{P}{v \bullet h \bullet t}$$

Some studies substitute laser beam diameter (mm) for hatch distance. It is crucial to align the hatch distance with the laser beam diameter to ensure a specific overlap ratio is maintained. This alignment is key to ensuring uniform application of the laser's heat during the material fusion process. By precisely matching the hatch distance to the diameter of the laser beam, the

technique ensures sufficient overlap between successive laser passes, as shown in Figure 16. Adequate overlap is vital for the consistent melting and solidification of the powder, which significantly affects the density, structural integrity, and overall material quality of the final product. Therefore, this alignment is not just a technical detail but a critical factor that greatly influences the success of the LPBF process in producing components that meet specific mechanical and physical standards. [41][36].

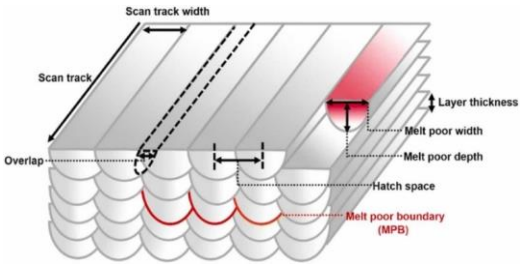


**Figure 16:Graphical representation of L-PBF process parameters[36]**

Understanding the significance of VED is pivotal in addressing challenges arising from factors like laser configurations, powder characteristics, and the intricate physics surrounding energy absorption and material solidification. These factors are known as the source of defects, such as porosities, incomplete fusion, and cracks, which detrimentally affect the quality and suitability of fabricated parts. Research indicates that categorizing VED into distinct ranges yields three sets of outcomes. Low VED, as illustrated in Figure 17, is associated with the occurrence of incomplete fusion in a single scan track, which, by being repeated in a printed part, will apper as Lack of Fusion (LoF) defects. Achieving an optimized VED tailored to the specific material target results in dense, nearly defect-free components. Conversely, high VED values introduce the issue of keyhole porosity. The subsequent section delves into a comprehensive explanation of defects related to PBF processes [40].

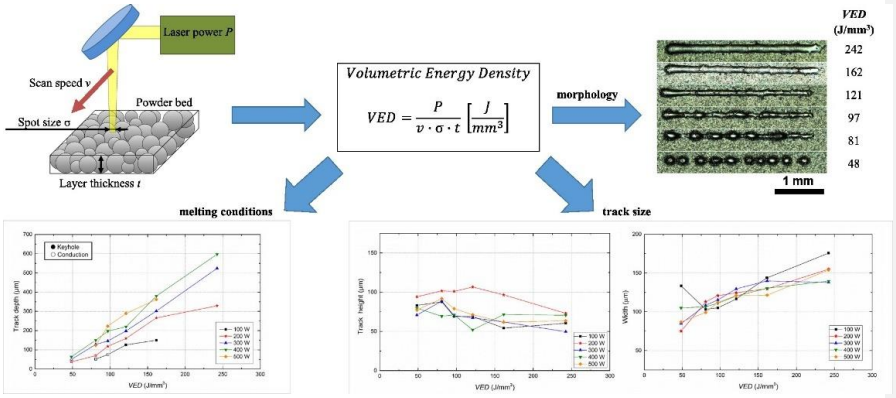


**Figure 17: VED formula and its effect on final result[41]**

L-PBF offers a plethora of advantages in the AM. L-PBF's efficiency in rapid part production, reduced material waste, and the potential for lightweight design further contribute to its appeal [36]. Additionally, L-PBF process can be employed to produce a wide range of various metals, expanding its applicability across diverse sectors. Overall, L-PBF's versatility, precision, and suitability for high-value, low-volume manufacturing make it a transformative technology with far-reaching implications across multiple industries [32].

### 1.2.3 Defects formation in PBF technologies

Different defects may originate during the process. Although, in some cases, post-processing techniques are suitable to mitigate or remove defects from PBF-produced parts (e.g., hipping), improving the quality of the as-built parts is fundamental to meet stringent and challenging industrial requirements. Understanding the defects and their causes represents the first step to design process monitoring and control tools. Defects commonly observed in AM parts exhibit different morphologies linked to their formation mechanisms. The compatibility of the material with the chosen AM technique also plays a pivotal role in defect formation [42][43].

*Porosity*

As shown in Figure 18, three common types of volumetric defects or porosity—lack of fusions (LoFs), gas-entrapped pores (GEPs), and keyholes (KHs)—exhibit distinct geometries characterized by parameters including maximum dimension, roundness, sparseness, and aspect ratio, among others. These defects act as stress risers and detrimentally affect the mechanical properties of additively manufactured parts, particularly in terms of fatigue resistance [44][22][40].

LoFs typically form due to insufficient overlap between adjacent melt pools, between layers, or along laser tracks. This inadequacy can result from insufficient energy input or excessively large hatch distances [45][46]. Conversely, KHs form under overheating conditions due to the "pinch-off" phenomenon occurring at the bottom of depressions within the melt pool for very high energetic process parameters. GEPs shown in Figure 18, can originate from two primary factors: the production process and the characteristics of the powder used. In the production process, these pores, resembling "bubbles" of inert gas trapped within the melt pool or between powder particles, emerge due to a complex interplay of several factors. These contributing factors include buoyancy, the Marangoni force, turbulence induced by vapor recoil, and the rapid solidification front during the AM process [42]. When considering the characteristics of the powder used, gases can inadvertently be introduced during the preparation of the powder material [47]. This is particularly relevant in the case of gas atomized powders that are protected by inert gases such as argon or helium. These gases have the potential to introduce GEPs into the component, which can significantly impact its quality and structural integrity.

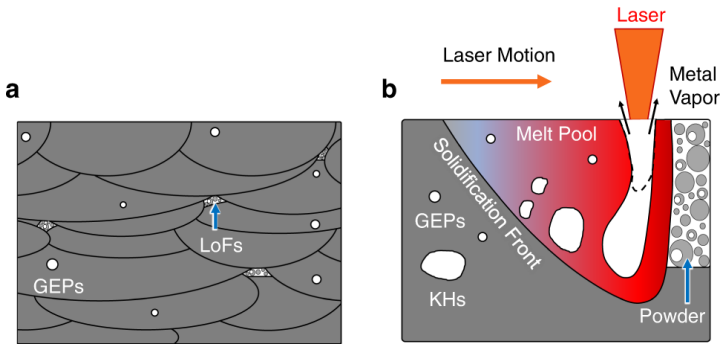


**Figure 18: a Formation of LoFs and GEPs. B Formation of KHs and GEPs[42].**

In L-PBF, these volumetric defects may contain shielding gases, such as argon (Ar), which are often insoluble in the metal. Consequently, removing these defects poses significant challenges, if not impossibilities, as it would require the complete expulsion of such gases throughout the metal bulk.

*Residual stresses, cracking, and delamination*

Residual stresses in PBF can stem from two distinct mechanisms, namely the thermal gradient mechanism and the cooling phase of molten top layers. When tensile stress surpasses the ultimate tensile strength of the solid material at a specific point and temperature, stress relief through fracturing can result in cracking phenomena, as shown in Figure 19. Various material-dependent mechanisms leading to cracks in PBF have been examined by different researchers. Delamination, a specific case of cracking, involves the initiation and propagation of cracks between adjacent layers. Delamination occurs when the residual stresses exceed the bonding strength between the top layer and the underlying one [43].

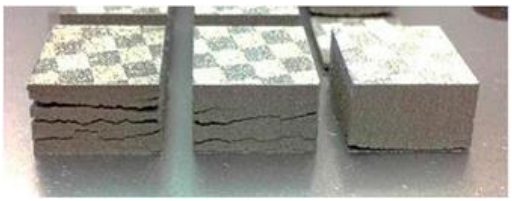

**Figure 19: Example of severe delamination and cracking[43]**

*Microstructural inhomogeneities and impurities:*

PBF processes involve highly localized high-heat inputs during very short beam-material interaction times that will significantly affect the microstructure of the part. This can lead to the evaporation of some elements, ultimately altering the properties of the final alloy[34]. Microstructural inhomogeneities or non-equilibrium microstructures, together with the aforementioned defects, may have a detrimental effect on the mechanical and functional performances of the part. Inhomogeneities of the microstructure include (i) impurities, (ii) grain size characteristics, and (iii) crystallographic textures. Impurities in the material comprise inclusions, contaminations from other materials, and formations of surface oxides [43].

While optimizing AM process parameters is a crucial step to minimize defect size and population during fabrication, certain post-processing techniques like Hot Isostatic Pressing (HIP) can effectively eliminate defects [45]. The HIP process, in line with conventional powder metallurgy and foundry techniques, has become a significant contender [46][47][51].

## 1.3 Hot Isostatic Pressing (HIP)

This method has garnered significant attention in the manufacturing industry due to its capability to enhance the performance of metallic components through defect reduction and microstructural improvement [48][49][50]. The HIP process is accomplished by applying high temperature and pressure uniformly to a material in a sealed container filled with an inert gas, such as argon or helium, to achieve a uniform density and reduce any internal voids or defects [47][48][51].

The furnace employed in the HIP procedure comprises essential components: a heater generating high temperatures, a thermal barrier that sustains the furnace's internal high temperature and safeguards the pressure vessel from its effects, along with a temperature monitoring system. The fundamental furnace concept is depicted in Figure 20. HIP furnaces harness a combination of three heat transfer mechanisms: conduction, convection, and radiation. Notably, conduction's impact is limited in HIP due to argon's low thermal

conductivity, the prevalent gas. Convection and radiation stand as the primary contributors to heat transfer. Argon and helium are the predominant gases utilized for pressure transmission in the HIP process [51]. In addition to reducing porosity, HIP can also be used as a heat treatment method to design the microstructure and improve the mechanical properties of metallic components [52][53][54][55].

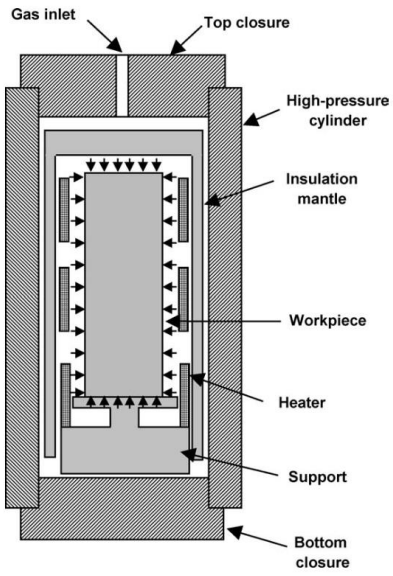


**Figure 20: Schematic drawing of HIP unit[51]**

As illustrated in Figure 21, HIP serves also as a production method for various metals [48][50]. This dual role makes HIP a versatile approach for manufacturing metal components. In this context, two prevalent methods for producing metal parts utilizing HIP are powder metallurgy and investment casting. These techniques leverage the capabilities of HIP to achieve densification, particularly when it is performed via the encapsulation method, encompassing a range of diverse powders(Table 1). HIP's ability to consolidate and densify materials under high temperature and pressure conditions plays a pivotal role in enhancing the quality and performance of metal components, making it an indispensable technology in advanced manufacturing [56][57][58][59].

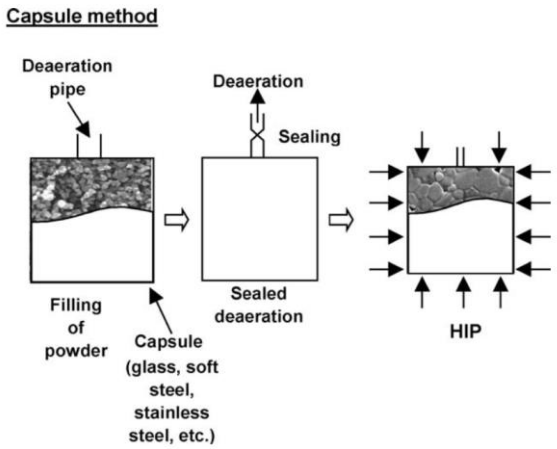


**Figure 21: Schematic drawing of encapsulation method[51]**

**Table 1: Results of HIP densification by encapsulation method for different powders**

| Powder | Capsule | HIP | | | Relative density (% T.D.) |
|---|---|---|---|---|---|
| | | Pres. (MPa) | Temp. (°C) | Time (h) | |
| $Si_3N_4$ | Pyrex | 80 | 1800 | 1 | 97.0 |
| BN | Silica | 145 | 1850 | 1 | 97.1 |
| TiN | Silica | 145 | 1850 | 1 | 98.9 |
| SiC | Silica | 145 | 1850 | 1 | 87.0 |
| $B_4C$ | Pyrex | 90 | 1900 | 1 | 96.3 |
| TiC | Pyrex | 90 | 1900 | 1 | 93.0 |

In the context of HIP applied to high porous bulk samples or capsules produced by PBF, it is important to address the deformation and shrinkage phenomena resulting from high porosity within these components. The presence of significant porosity in PBF-produced capsules can lead to several challenges during the HIP process. As the capsules undergo HIP treatment, the high-pressure and high-temperature conditions exerted by the working medium cause the entrapped gas within the pores to compress [65][66]. While this compression aids in densifying the material and reducing porosity, it also generates internal stresses [60]. These internal stresses can contribute to deformation and shrinkage of the capsules, as shown in Figure 22 and Figure 23 [61]. The extent of deformation and shrinkage can vary depending on factors such as the initial porosity level, the HIP parameters, and the material characteristics. Therefore, careful consideration and optimization of the HIP process parameters are essential

to minimize deformation, ensure dimensional stability, and effectively reduce porosity in PBF-produced capsules, ultimately enhancing their mechanical properties and suitability for various applications [60].

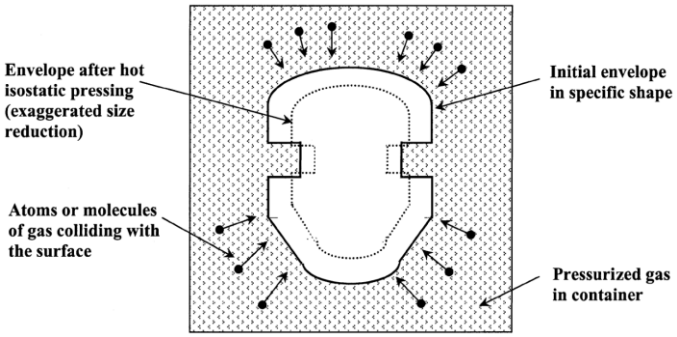


**Figure 22: Isostatic pressing causes a photographic reduction in the shape of an encapsulating envelope and the densifying powder that it contains.[49]**

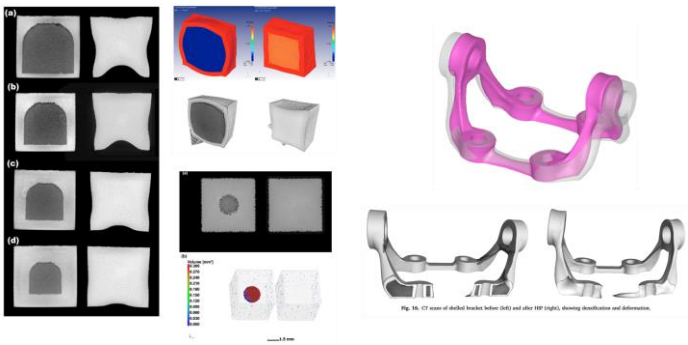

**Figure 23: The effect of HIP on capsulated Ti alloys of deformationand densification[62][63]**

The underlying mechanism for mitigating and eliminating specific types of voids or pores within materials revolves around the diffusion process. To achieve effective consolidation, it is imperative that the pores within the material are in an isolated state. Isolated pores respond favorably to HIP treatment by reducing size or closing entirely. However, the efficacy of HIP in addressing porosity diminishes when dealing with interconnected or non-isolated pores, as the diffusion of material to these pores becomes challenging. Thus, the types of pores that can be effectively closed or reduced by HIP predominantly encompass those in an isolated state, underscoring the significance of pore isolation for successful pore elimination and densification

during the HIP process [64]. This nuanced understanding of pore behavior underpins the optimization of HIP techniques for enhancing the mechanical properties of materials, particularly in applications where porosity reduction is a critical requirement. It is essential to consider that as defects within the material shrink, they can generate back pressure within these voids. This back pressure acts in opposition to the pressure exerted by the working medium, hindering the complete closure of defects. Notably, due to this internal pressure, defects have been observed to undergo regrowth during subsequent post-HIP heat treatments. This phenomenon underscores the complex interplay of forces and conditions within the material during HIP and highlights the importance of carefully managing the process parameters and subsequent treatments to ensure effective defect closure and material densification [42][65][66][67].

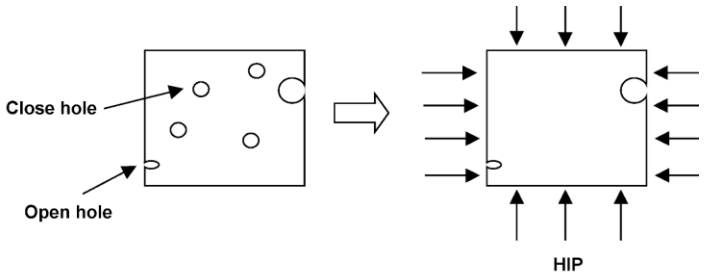


**Figure 24: Schematic of capsule-free method[51]**

Table 2 shows typical HIP pressure and temperature based on the material, compared to their melting point and yield stress at room temperature. The potential resulting defect-free material is suitable for precision engineering applications that require low surface roughness and high durability [60][65][66][67].

**Table 2: Typical Hipping Pressures and Temperatures[50]**

| Material | Melting Point $T_m$ (°C) | Yield Stress at Room Temperature (MPa) | Hipping Temperature (°C) | Hipping Pressure (MPa) |
|---|---|---|---|---|
| Al and its alloys | 660 (Al) | 100 to 627 | 500 | 100 |
| $Al/Al_2O_3$ | — | — | 300 | 350 |
| Cu and its alloys | 1083 (Cu) | 60 to 960 | 800 to 950 | 100 |
| Be and its alloys | 1289 (Be) | 240 | 900 | 103 |
| Nimonic and superalloys | 1453 (Ni) | 200 to 1600 | 1100 to 1280 | 100 to 140 |
| Hydroxyapatite | — | — | 1100 | 200 |
| Mg/Zn ferrite | — | — | 1200 | 100 |
| TiAl | — | — | 900 to 1150 | 35 to 200 |
| $Ti_3Al$ | — | — | 925 | 200 |
| Ceramic superconductors | — | — | 900 | 100 |
| Steels | 1536 (Fe) | 500 to 1980* | 950 to 1160 | 100 |
| Ti and its alloys | 1670 (Ti) | 180 to 1320 | 920 | 100 |
| $Al_2O_3$ | 2050 | 5000 | 1500 | 100 |
| $Al_2O_3$/glass | — | — | 1400 | 100 |
| $Al_2O_3$/TiC | — | — | 1935 | 150 |
| $Al_2O_3/ZrO_2$ | — | — | 1500 | 200 |
| SiC | 2837 | 10,000 | 1850 | 200 |
| $B_4C$ | — | — | 2000 | 200 |
| WC/Co | 2867 | 6000 | 1350 | 100 |

*Low-alloy steels (water quenched and tempered).

Many studies observed that HIP treatment resulted in significant consolidation of the material, crack elimination, and major porosity reduction in PBF-produced parts. In a study conducted by Yan et al. [66], it was demonstrated that HIP treatment had a remarkable effect on the microstructure and compressive properties of L-PBF-fabricated Ti6Al4V lattice structures. The study showed a significant reduction in internal porosity from 5.9% in the as-built condition to 0.5% after HIP treatment. Furthermore, a major improvement in strength and fracture strain was observed in comparison to the as-fabricated condition [66]. In the case of the MoSiBTiC multiphase alloy, HIP treatment has been found to effectively decrease the length of microcracks due to TiC nanoparticles bridging, which occurs as a result of an increase in temperature during the process. This temperature increase also plays a significant role in healing internal microcracks. In addition, the content and grain size of the TiC phase gradually increased with rising temperature. The study showed that the HIP treatment improved the room-temperature fracture toughness of the alloy, indicating that the combination L-PBF process and HIP post-treatment is a promising method for fabricating high-performance refractory MoSiB-based components [54]. Tillman et al. [72] conducted a study using various techniques, including micro X-ray computed tomography (XCT) and scanning electron microscopy, to examine the impact of HIP on an IN718 component manufactured by L-PBF. The study found that the combination of high pressure and high temperature provided in HIP can lead to the production of materials with superior properties by densifying the majority of pores. However, some pores cannot be densified due to the entrapped argon gas from the L-PBF process [72].

In summary, HIP is a highly effective post-processing technique for enhancing mechanical properties by reducing or eliminating defects in components produced through different AM techniques for different materials. HIP eliminates porosities and improves material homogeneity, improving mechanical performance.

## 1.4 This work

In the landscape of contemporary additive manufacturing (AM), the preservation of alloy components and material integrity is a palpable challenge, particularly concerning the production of TiAl components. A salient concern arises during high-temperature preheating, where the evaporation of aluminum—an essential element in TiAl—poses a significant issue during the EB-PBF process. To address this issue, a novel approach has surfaced as a potential solution. In the initial phase, we produced a range of TiAl massive samples via EB-PBF using different process parameters to identify the optimized process parameter for achieving fully dense yet partially porous massive samples. For us, a safe level of porosity entails a level that can be fully densified after HIP treatment. At this stage, we also considered the well-established phenomenon of the banded microstructure of TiAl when produced by EB-PBF. To investigate the controllability or preventability of this heterogeneity in the TiAl microstructure, we embarked on the development of a new technique for producing TiAl capsules by EB-PBF and densifying them via HIP.

Departing from the traditional method of scanning powder within the samples, this innovative technique employs HIP to consolidate capsules with dense borders and pre-heated powder or rapidly scanned powder inside. The integration of EB-PBF and HIP aims to achieve two primary objectives: creating fully dense TiAl capsules while minimizing the loss of aluminum content within the material matrix. This inventive strategy has the potential to reshape TiAl alloy manufacturing by offering the possibility of producing high-density TiAl capsules while safeguarding critical alloy components, thus enhancing overall material performance. Secondly, it is crucial to recognize that this approach has limitations. Densification through HIP introduces challenges such as distortion and deformation, often resulting from the HIP process itself and subsequent shrinkage, which must be considered and controlled.

In the subsequent phase of this research, we focused on investigating the impact of HIP on the densification of Ti64 components, as well as the duration of HIP on its microstructure. The main goal was to evaluate the effects of the HIP process on densely produced samples through L-PBF. The secondary objective involved understanding the influence of time as a HIP parameter and its effect on the microstructure of Ti64. Additionally, this effort aimed to elucidate the role of design parameters in managing deformation and shrinkage during capsule production, followed by HIP densification.

# Chapter 2

# Materials and Methods

## 2.1 TiAl

Gamma Titanium Aluminide (TiAl), commonly referred to as gamma TiAl, is an intermetallic compound that has attracted significant attention in the field of advanced materials. TiAl alloys are well adapted to high-temperature applications and are known for their considerable creep properties, excellent resistance to oxidation, low density, and high specific yield strength [68]. This material has gained prominence in various industries due to its unique combination of attributes, and it has shown great promise in additive manufacturing, specifically in powder bed-based techniques like EB-PBF [69]. The engineering properties of advanced γ-TiAl based alloys rely significantly on the microstructural constituents, which can be regulated through powder composition, EB-PBF processing parameters, and heat treatment conditions [34].

One of the key characteristics of gamma TiAl is its low density, approximately half that of Ni-based superalloys. This property makes it an attractive choice for applications where weight reduction is crucial, such as in the aerospace industry [70]. The material's high oxydation resistance and high-temperature durability have also led to its exploration in automotive applications, including exhaust systems and engine components. Additionally, gamma TiAl has demonstrated potential in fields such as power generation, chemical processing, where its unique properties offer significant advantages [71][72]. The TiAl phase achieves higher resistance against oxidation than Ti3Al phase thanks to a higher content of aluminium. The creep limit for TiAl alloys is at 1000 °C, and the resistance to high-temperature oxidation is up to 900 °C [73][74][75].

The advancement of AM has opened up a host of possibilities for the production of intricate components using gamma TiAl. Among the powder bed-based techniques, EB-PBF stands out for its precise control over the melting and solidification processes, enabling the manufacturing of complex geometries with optimized material properties. The A2X machine (ArcamEBM, GE Additive, Sweden) is particularly well-suited for handling TiAl alloys due to its capability for high vacuum processes at elevated temperatures, addressing the challenges posed by high melting points, complex phase diagrams, and susceptibility to contamination, such as oxidation. The aerospace sector, in particular, is leveraging the potential of AM to produce high-performance components, with intricate and lightweight TiAl turbine blades serving as successful examples. The EB-PBF process optimizes production efficiency by streamlining the fabrication of near-net shape parts and minimizing waste material through efficient powder recycling [76][77]. One of the most critical advantages of using the EB-PBF technique for producing gamma TiAl alloys is the preheating temperature, which lowers residual stresses and promotes the successful, crack-free building of components. It is also worth mentioning the issue of aluminum loss during the process, which can be detrimental to the final properties of the components [78]. This thesis proposes a method to mitigate this critical issue.

The potential use of gamma TiAl alloy in aero turbine applications has motivated its processing using EB-PBF manufacturing. Research conducted by Baudana et al. [77] has shown that among the AM technologies, EB-PBF is particularly suitable for fabricating Titanium aluminide. Studies conducted by Biamino et al. [76] have demonstrated that Ti-48Al-2Cr-2Nb fabricated using EB-PBF exhibits promising characteristics, such as a homogeneous microstructure. However, it should be noted that some studies have highlighted the limitations of AM-built gamma TiAl in terms of achieving fine microstructure and desired mechanical properties [15][77]. However, the mechanical properties of γ-TiAl alloys are strongly dependent on their microstructure, which derived from the thermal history of the components [79]. Based on the heat treatments, the TiAl based alloys present four different microstructures [77]:

- Near gamma microstructure
- Duplex microstructure
- Nearly fully lamellar microstructure
- Fully lamellar microstructure

In general, the duplex structure is preferable if is necessary a high ductility, tensile strength and longer fatigue life, while the fully lamellar structure is needed when the applications require a high toughness and creep resistance [69]. Figure 25 reports the TiAl phase diagram with the possibile microstructures based on the different heat treatment temperatures.

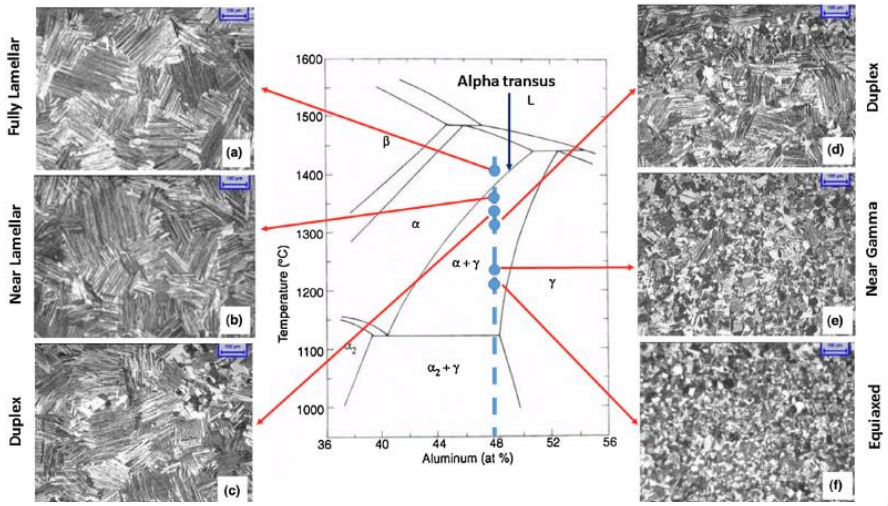


**Figure 25: The typical microstructure of TiAl-alloys obtainable with different heat treatment recipes. In particular, fully lamellar (a), near lamellar (b), duplex (c)(d), near gamma (e), and equiaxed (f) [77].**

An annealing treatment above the Alpha transus temperature leads to a fully lamellar microstructure. Adjusting the annealing temperature, it is possible to obtain different lamellar/equiaxed ratios, passing from a near lamellar structure to a duplex structure. With

lower annealing temperatures, it is possible to obtain near gamma structure and an equiaxed structure, consisting of globular gamma grains [77].

The main challenge in working with this material is that, despite the many advantages associated with EB-PBF, certain types of defects have been observed in parts produced using this technique.

By leveraging AM techniques like EB-PBF, gamma TiAl can be utilized to create lightweight, high-performance parts tailored to specific applications. Although challenges such as achieving fine microstructure, controlling defects, and ensuring material integrity for reliable mechanical properties exist, ongoing research and development efforts aim to overcome these obstacles and further enhance the capabilities of gamma TiAl produced through EB-PBF [80][81][64].

## 2.2 Ti Alloys

Ti6Al4V, commonly known as Ti64, is a commercially significant titanium alloy with a rich historical background. Developed in the 1940s through the pioneering work of William J. Kroll and his Kroll process, this alloy revolutionized the availability and cost-effectiveness of titanium [82]. Today, Ti6Al4V has been widely utilized in aerospace, automotive, and medical industries for its exceptional mechanical properties, including strength, corrosion resistance, and biocompatibility [83].

The microstructure of Ti6Al4V plays a crucial role in determining its mechanical properties. This alloy consists of approximately 90% titanium (Ti), 6% aluminium (Al), and 4% vanadium (V), with trace amounts of other elements[84]. It is characterized by an alpha-beta structure, with alpha-phase titanium grains and a beta-phase interstitial solid solution. The specific heat treatment and processing conditions influence the distribution and morphology of these phases, ultimately affecting the alloy's mechanical performance[85]. Figure 26 reports a scheme to explain the microstructure obtainable based on the phase diagram.

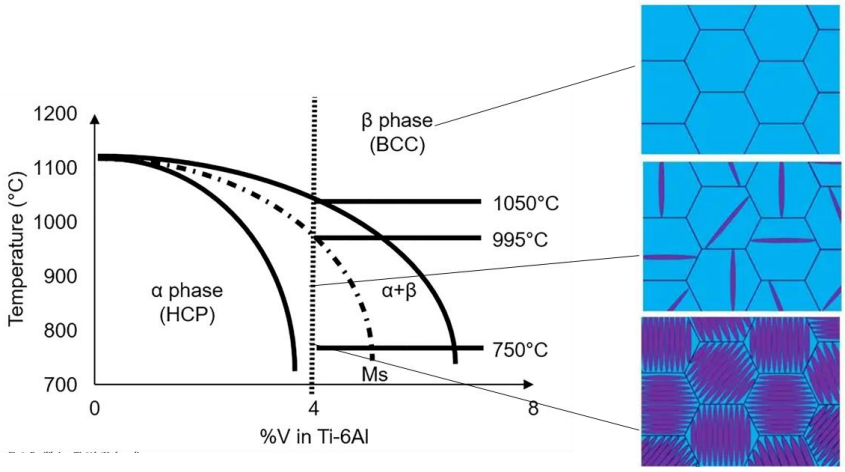


**Figure 26: Phase transformations of Ti6Al4V [21].**

The alpha-phase in Ti6Al4V provides good strength and ductility, while the beta-phase contributes to its high-temperature stability. The distribution and size of the alpha and beta phases can be controlled through various heat treatment methods, such as solution treatment, quenching, and aging. This allows for tailored microstructures and desired mechanical properties, making Ti6Al4V a versatile alloy for a wide range of applications [86].

The microstructure of Ti6Al4V is influenced by the AM process used for its fabrication, such as L-PBF [87]. In fact, Ti6Al4V can be processed by L-PBF obtaining high densification level. The rapid solidification and cooling rates inherent in the L-PBF process can result in unique microstructural characteristics, such as columnar grains, fine dendritic structures, and localized phase transformations.

Understanding and controlling the microstructure in L-PBF-fabricated Ti6Al4V components is crucial to ensure their mechanical integrity and performance [88][89][37]. In the work of Zafari et al. [87], they studied the microstructural changes of Ti6Al4V alloy with the variation of different process parameters. Figure 27 shows a TEM image of a fully lamellar structure with the alternation of beta and alpha phases. Additionally, studies by Wang et al. and Thijs et al. have demonstrated that process parameters such as laser power, scanning speed, and layer thickness significantly influence the microstructure, leading to variations in grain size and phase distribution, which in turn affect the mechanical properties of the alloy[90][91]. These findings highlight the importance of optimizing process parameters to achieve desired microstructural characteristics in Ti6Al4V components.

**Commented [GM1]:** The literature survey could be improved as required by reviewer Fabrizio Sarasini.

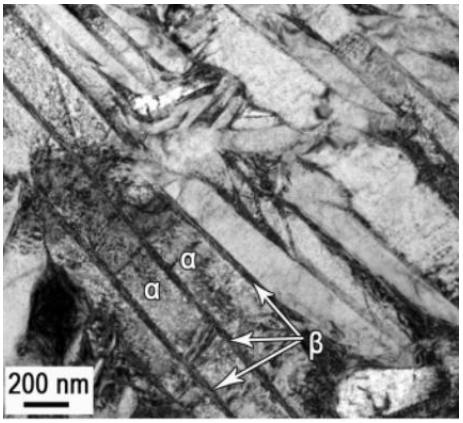


**Figure 27: TEM image of a fully lamellar Ti6Al4V obtained with LBPF** [87]**.**

## 2.3 Sample production

### 2.3.1 AM machines

*EB-PBF: A2X Archam*

The Arcam EB-PBF A2X machine is designed for material and process development. Featuring a development mode option, it allows for greater control over machine and process parameter settings within the machine software, facilitating advanced process development. With its robust build chamber engineered to endure process temperatures exceeding 1100°C, it can produce crack-prone materials like TiAl alloys.

The A2X operates in a vacuum, ensuring a clean and controlled environment that minimizes contamination risks. It leverages electrons as energy carriers, enabling deep energy penetration and minimal reflection in the powder, thereby optimizing material studies. Its build chamber, designed to withstand process temperatures of over 1000°C, expands the possibilities for creating new crack-prone alloys, with a maximum build size of 200 x 200 x 380 mm (W x D x H). Detailed technical data are reported in Table 3 [92].

**Table 3: Arcam A2X Technical Data**[92]

| Specification | Detail |
|---|---|

| | |
|---|---|
| Max. build size | 200 x 200 x 380 mm (W x D x H) |
| Max. beam power | 3kW |
| Cathode type | Tungsten filament |
| Min. beam diameter | 250 µm |
| Max. EB translation speed | 8,000 m/s |
| Active cooling | No |
| Minimum chamber pressure | 5 x 10^-4 mbar |
| Typical build atmosphere | 2 x 10^-3 mbar (partial pressure of He) |
| He consumption, build process | 1 liter/h |
| He consumption, ventilation | 50-75 liters/build cycle |
| Power supply | 3 x 400 V, 32 A, 7 Kw |
| Size approx. | 1,850 x 900 x 2,200 mm (W x D x H) |
| Typical process temperature range | 600-1,100°C |
| Weight | 1,700 kg |
| CAD interface | Standard: STL |
| Materials available | Arcam EBM Ti6Al4V Grade 5, P-Mtrl; Arcam EBM Ti6Al4V Grade 23, P-MtrlA; Arcam EBM Nickel alloy 718, D-Mtrl; Arcam EBM TiAl, D-Mtrl |


**Figure 28: Arcam A2X** [92]

*L-PBF MetalFAB1*

MetalFAB1 stands as a pioneering integrated metal additive manufacturing system tailored for high-end industrial applications within rigorous sectors such as aerospace, medical, high-tech equipment, tooling, and automotive industries. The MetalFAB1 (Figure 29) three-module version serves as the entry-level production model, engineered for fully automated and secure production of either single large parts or small series production. The incorporation of the Exchange Module and Robot streamlines the handling of both the build plate and finished products, eliminating the need for manual labor and minimizing direct contact with metal powders during regular production operations. Furthermore, the system ensures automatic system and laser calibration between build jobs, ensuring the utmost reproducibility and productivity. For heightened production rates of large parts, the MetalFAB1 system can be equipped with additional lasers, while the option for a second AM Core Module enables increased productivity and autonomous job changes. Additional modules catering to new

materials (AM Core Modules) and post-processing (Storage and Heat Treatment) further augment the system's capabilities, providing a comprehensive solution for various industrial demands. Additional technical details are shown in

Table 4 [93].

**Table 4: MetalFab1 Tecnical Data** [93]

| Specification | Detail |
|---|---|
| Process type | Laser Beam Powder Bed Fusion |
| Net build envelope | 420 x 420 x 400 mm (16.5 x 16.5 x 15.7 In) |
| Laser | Yb fibre lasers 500W (1kW under development) |
| Number of Lasers: | 1 to 4 full field, preventing laser overlap regions |
| Configurability | Configure 3 up to 11 modules for more productivity or post-processing automation |
| Build plate | Automated levelling and positioning |
| Powder handling | Automated extraction, sieving and recycling during the build cycle |
| Autonomous operation | 112 hrs), maximum 8 build jobs |
| Productivity | Up to 1,000 cm3/hr (with 4 lasers, depending on material) |
| Accuracy | < \|0.050\| + 0.002 x part length\| [mm] |

| | |
|---|---|
| Reproducibility | < \|0.050\| [mm] |
| Layer Thickness | 20-100 µm |
| Optical calibrations | In-line, automated, laser-2-laser and focus |
| Safety | No direct powder exposure during regular operations |
| Storage positions | 8 empty build plates |
| Job preparation | Off line build set up, Dynamic Laser Assignment |
| Remote access & monitoring | Yes, through Additive World Platform |
| Materials | Titanium (Ti6Al4V), Aluminium (AlSi10Mg), ScalmAlloy, Stainless Steel (316L), Inconel (IN718), Tool Steel (1.2709) |
| Preheating | 175 °C |


**Figure 29: MetalFAB1 by Additive Industries**

### 2.3.2 TiAl Sample Design and Printing

The TiAl powder used for the samples production was produced via inert gas atomization, with a nominal composition of Ti–49.06Al–1.88Cr–1.98Nb and supplied by Arcam. The particle size distribution was from 40 to 150 µm. The samples were realized with an Arcam A2X EB-PBF machine, equipped with a build volume of 200x200x380 mm and an electron beam max power of 3 kW. Two jobs were performed, both with a 90 µm layer thickness. The first job was related to bulk cubic samples 18x18x18 mm. The second one involved the production of capsule samples (dimension 18x18x18 mm) with the design represented in Figure 30. The capsules are designed by producing walls with standard process parameters in order to obtain a wall with high densification while the inner part contains partially melted powders or preheated powders in some cases. The presence of a dense contour is important to avoid defects that can inhibit the consolidation by HIP treatment.

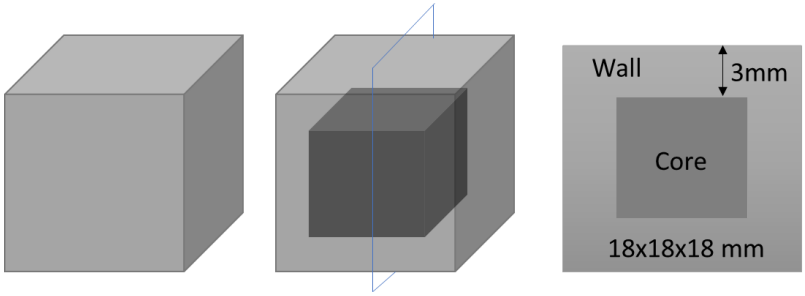


**Figure 30: Capsules design.**

The scanning strategy applied involved a rotation of 90 ° between consecutive layers and the temperature set during the preheating phase was 1050 °C, for both jobs. The process parameters related to the two different batches of samples will be described in the corresponding results sections.

### 2.3.3 Ti64 Sample Design and Printing

The Ti6Al4V powder was supplied by Tekna, with a nominal composition of Ti – 6-6.5%Al–3.5-4-5%V–<0.25%Fe–<0.13%O and produced via plasma atomization. The particle size distribution was from 15 µm to 45 µm . A similar approach was followed, performing a job of bulk samples and a second one of capsules. In this case, the L-PBF machine used was a MetalFab1 by AM industries equipped with a Yb fibre laser with a max power of 500W. The available build envelope was 420x420x400 mm with the possibility to heat up the building platform up to 175 °C. The bulk samples were 10x10x10 mm, while the capsules were designed following the scheme in Figure 31 with different dimensions (Figure 32 Figure 33).

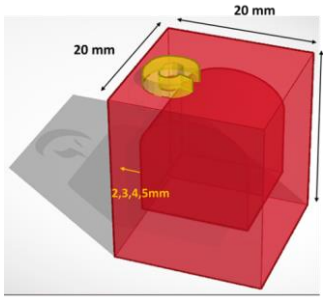


**Figure 31: A schematic representation of Ti64 capsules design.**

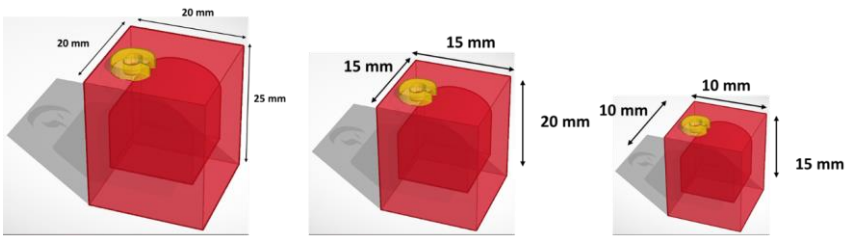


**Figure 32: Dimension of Ti64 capsules design.**

## 2.4 Samples Characterization

The following section provides a comprehensive overview of the sample characterization procedure implemented in this study. Each step of the procedure, ranging from the cutting and polishing of the samples to the application of various analysis methods, will be elucidated. This standardized procedure was consistently applied to both the TiAl and Ti6Al4V samples investigated in this thesis work.

### 2.4.1 Metallographic Preparation

The metallographic preparation started with the cut of the samples along the building direction. A cutting machine BRILIANT 220 (Figure 33) equipped with a cermet blade was used to carry out this goal.

**Figure 33: Cutting Machine BRILIANT 220**

To ensure a flat and planar surface of the samples, a grinding step was conducted using a MECATECH 234 polishing machine (Figure 34). The machine consisted of a rotating plate equipped with SiC (silicon carbide) papers of increasing grit sizes, ranging from #320 to #2500. The rotational speed of the plate was set at 250 RPM. During the grinding process, it was crucial to maintain a continuous lubrication of the rotating plate. This lubrication helped reduce friction between the paper and the sample, thereby minimizing any potential increase in the surface temperature of the samples. By controlling the temperature, the integrity and quality of the samples were preserved. Following the grinding step, a polishing procedure was carried out to achieve a mirror-like surface finish. A 0.03 µm silica suspension was used for this purpose,

diluted at a ratio of 1:1 with distilled water. After the polishing step, the samples underwent a thorough cleaning process. They were washed under running water to remove any residual silica suspension from the surface. Subsequently, the samples were carefully dried to eliminate any remaining water or contaminants. This meticulous sample preparation protocol guaranteed the attainment of a highly polished and pristine surface, devoid of any residual silica or other contaminants. Such a surface condition was essential for accurate and reliable subsequent analyses, allowing for precise characterization and observation of the samples. For microstructural analyses, the samples were chemically etched with Kroll's solution for 7-10 seconds.


**Figure 34: Polishing Machine MECATECH 234**

### 2.4.2 Light Optical Microscope

The light optical microscope (LOM) observations were useful to determine the defects of the samples as well as the main microstructural features after chemical etching. A LEICA DMI 5000 M light optical microscope was used. For the evaluation of the porosity, the LOM images were recorded with high contrast in order to highlight better the defects on the surface. This setting was essential for the further image analysis described in the next section.

To ensure comprehensive coverage of the sample surface, an average of twenty images were collected for each sample, utilizing different magnifications ranging from 50X to 200X. Specifically, five images were captured at 50X and 100X magnification, while 10 images were collected at 200X magnification. Moreover, the microstructural analyses were performed after the chemical etching previously described. In this case, different images for different magnifications were acquired (from 50x to 1000x) in order to have a complete overview of the microstructural features.

**Figure 35: LEICA DMI 5000 M optical microscope.**

*Post Processing Analysis*

The post-processing analysis was necessary to analyse the images to provide different information such as defects amount (related to the relative density) and phases presence. To carry out the analysis was used ImageJ, an open-source image analysis software developed by the National Institute of Health, USA. It follows the description of the image analysis applied for the relative density definition of the samples:

- **Step 1,** open the image: the image previously acquired with the optical microscope is opened with ImageJ and it is possible to work on it.
- **Step 2,** 8-bit conversion: through a specific command, the image is converted to 8-bit i.e., in a greyscale image.
- **Step 3,** pixel value threshold: with this command is possible to identify the pixel of the image with a specific value (black pixels) and separate them from the background (white pixels). In this way, it is possible to detect the defects (porosity) derived from the printing.
- **Step 4,** binary conversion: a new image is created from the previous threshold step. The new image is binary and now ready to be analysed.
- **Step 5,** image analysis: in this step the binary image is analysed returning the values of the percentage of black pixel over the background, corresponding to the porosity level of the sample.

All the processes just described are summarized in the scheme in Figure 36.

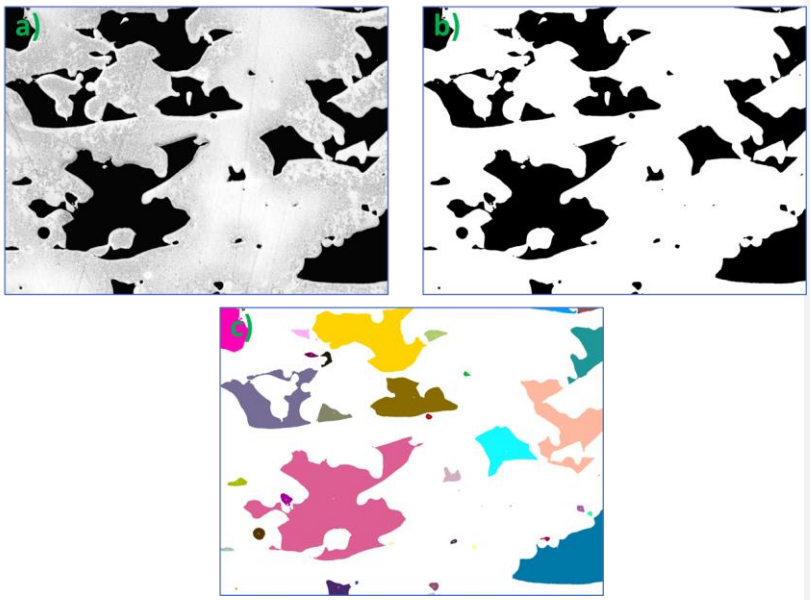


**Figure 36: A summary scheme of ImageJ analysis: original image (a), black and white version after threshold (b) and analysis phase with the particles detected coloured (defects) (c).**

### 2.4.3 Scanning Electron Microscope

The analysis of the samples was conducted using a Phenom ProX scanning electron microscope (SEM), as depicted in Figure 37. In addition, FESEM Tescan S9000G (Figure 38) was utilized to gather more information about phases and grains. Samples were mirror polished for this analysis. Since the investigation was always focused on the densified powder inside the capsules, all selected regions for analysis are in the core of samples in a randomly chosen manner. For more detailed analyses, the electron backscattered diffraction (EBSD) technique was employed, using a tilting angle of 70° and scanned at 20 kV and 10 nA. A step size of 0.8 µm was used for performing the EBSD analysis at a magnification of 500×. The EBSD analysis can be used to distinguish between phases with different crystallographic structures. Moreover, it can be used to determine the crystallographic orientations of the grains to identify the possible texture of grains.


**Figure 37: Phenom ProX SEM machine**

**Figure 38: TESCAN S9000G**

### 2.4.4 X-Ray Fluorescence

X-ray fluorescence (XRF) is a non-destructive analytical technique widely used to determine the chemical compositions of various materials, including metal alloys. By irradiating a sample with high-energy X-rays, XRF induces the emission of secondary (or fluorescent) X-rays that are characteristic of the elements present in the material. This method allows for the precise and rapid identification and quantification of elements, making it invaluable in quality control, material verification, and research applications. XRF's ability to analyze a broad range of elements, from sodium (Na) to uranium (U), combined with minimal sample preparation, enhances its utility in diverse fields such as metallurgy, geology, and environmental science.

### 2.4.5 X-Ray Diffractometer

XRD analyses were performed to study the phase changes in the different conditions. The instrument used for this purpose was an XRD diffractometer-X-Pert Philips PANalytical

Almelo, The Netherlands. The peak identification and data analysis were performed with the software X'pert Highscore, from the same company.

**Figure 39: XRD diffractometer-X-Pert Philips PANalytical.**

# Chapter 3

# Results and discussion

## 3.1 Titanium Aluminides Produced by EB-PBF

As discussed in the previous chapter outlining materials and methods for TiAl, intermetallic γ-titanium aluminide (TiAl) alloys have gained significant attention as promising materials for high-temperature applications, typically in the range of 600-750 °C. This heightened interest arises from their remarkable properties, including low density, high specific strength, excellent oxidation resistance, and resistance to creep deformation. These inherent qualities make intermetallic TiAl alloys particularly appealing for aerospace and aeronautical applications. For instance, the utilization of TiAl alloys in the production of low-pressure turbine blades has already demonstrated significant advantages, such as reduced fuel consumption compared to heavier Nickel-based superalloys, which have nearly double the density of TiAl alloys.

Traditionally, TiAl alloys have been primarily manufactured using casting methods, such as investment casting. However, in recent years, there has been increasing interest in employing AM techniques like EB-PBF for TiAl alloy production. This approach offers the distinct advantage of fabricating complex-shaped components without the occurrence of cracks in a single processing step. Nevertheless, it is essential to acknowledge that the process parameters, including beam current, beam speed, line offset, and melting strategy, can lead to aluminum (Al) evaporation during TiAl component production via EB-PBF. This evaporation phenomenon can introduce microstructural heterogeneity characterized by banded structures featuring regions with altered Al content, oscillating between depletion and enrichment. Consequently, these variations can manifest as discrepancies in mechanical properties.

The challenge posed by Al evaporation has led to the exploration of low-energy processing parameters to mitigate its effects. However, the utilization of such parameters carries the risk of generating substantial defects, such as lack of fusion, which can significantly compromise the mechanical properties of the component. Consequently, developing strategies to counteract Al loss and maintain high densification levels during the EB-PBF production of TiAl becomes imperative. The application represents a viable approach for consolidating defects, particularly for critical components destined for aerospace applications. Despite HIP's effectiveness in defect removal, it is pertinent to recognize that an inhomogeneous microstructure may persist in the heat-treated state, thus altering its mechanical performance.

For the TiAl alloys, specific heat treatment protocols can be tailored to achieve varying fractions of lamellar and equiaxed grains, thereby affording desired combinations of mechanical properties. For instance, annealing TiAl alloys at temperatures exceeding the alpha transus temperature, followed by rapid cooling, facilitates the generation of a fully lamellar microstructure. Conversely, reducing the annealing temperature below the alpha transus temperature results in microstructures characterized by near lamellar, duplex, near gamma, and

equiaxed grains. These variations enable the fine-tuning of properties, including creep resistance, fracture toughness, ductility at room temperature, and fatigue resistance. However, the presence of microstructural irregularities can detract from mechanical performance and promote the premature initiation of cracks within components.

This study has proposed an alternative approach to enhance the microstructural homogeneity of TiAl alloys, involving the creation of near-net-shape closed capsules filled with sintered powder using EB-PBF, followed by post-HIP processing. The successful execution of this stage was contingent on the insights gleaned from our initial investigative phase, wherein we generated massive samples with varying area energies to achieve different levels of porosity. Subsequently, subjecting these samples to HIP enabled us to identify the most suitable process parameters, optimal design, and geometry. These crucial findings paved the way for the subsequent phase of capsule creation. This approach presents a potential solution to the Al loss issue and holds promise for yielding a more uniform microstructure. However, investigations have revealed the persistence of microstructural features, such as previous particle boundaries (PPBs), within these capsules [94][95]. The presence of such features can significantly reduce the mechanical performance of the components.

### 3.1.1 Porosity

*Massive Samples*

The same HIP parameters were employed to all the samples. The HIP treatment parameters were a temperature of 1260 °C, a pressure of 170 MPa, and a dwell time of 4 h, followed by furnace cooling. By varying the levels of area energy (all printing parameters are shown in Table 5), we were able to observe distinct porosity trends in the generated bulk samples, as depicted in Figure 40. Notably, samples produced with lower AE exhibited the highest levels of porosity, particularly of the LoF type. As the AE increased, there was a corresponding decrease in the porosity percentage, ultimately leading to the achievement of fully dense components in their as-built condition. Upon subjecting this range of components to HIP, it became evident that the efficacy of the HIP process was directly influenced by the initial level and type of porosity in the as-built condition. As illustrated in Figure 40, samples with a higher percentage of LoF displayed reduced porosity levels after HIP treatment, although some residual porosity persisted. Conversely, samples created with more optimal area energy exhibited marked improvements post-HIP, nearly reaching full density. However, it is worth noting that this trend was not applicable to samples produced with higher AE levels, as these samples already displayed high density levels. These results allow us to identify the precise area energy required to generate samples with certain levels of porosity, thereby enabling the attainment of full density following HIP treatment.

**Table 5: Process parameters employed for producing the massive specimens**

| Samples | Beam Speed (mm/s) | Beam Current (mA) | Line Offset (mm) | Area Energy (J/mm²) |
|---|---|---|---|---|
| 1 | 2800 | 8 | 0.2 | 0.86 |
| 2 | 2800 | 10 | 0.3 | 0.71 |
| 3 | 3000 | 12 | 0.3 | 0.8 |
| 4 | 2800 | 10 | 0.2 | 1.07 |
| 5 | 2200 | 10 | 0.2 | 1.36 |
| 6 | 1600 | 10 | 0.2 | 1.88 |
| 7 | 4000 | 18 | 0.3 | 0.9 |
| 8 | 5000 | 18 | 0.3 | 0.72 |
| 9 | 1600 | 12 | 0.2 | 2.25 |
| 10 | 2800 | 10 | 0.1 | 2.14 |
| 11 | 1600 | 10 | 0.2 | 1.88 |
| 12 | 1600 | 10 | 0.2 | 1.88 |

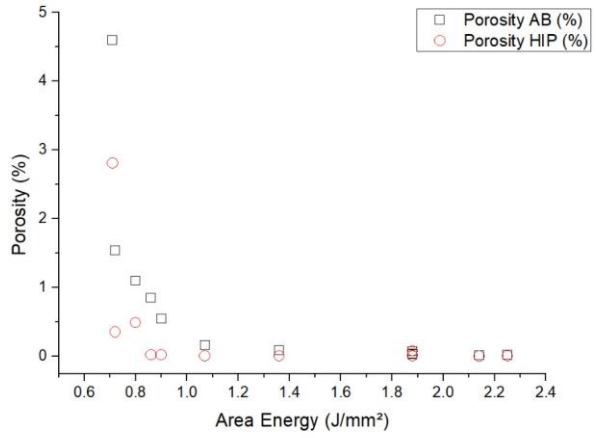


**Figure 40 Porosity Level vs. AE_ of the samples in the as-built and HIPed conditions by LOM analysis**

Figure 41 illustrates three distinct types of bulk sample candidates produced using varying levels of area energy, showcasing the corresponding levels and types of porosity present in the as-built condition (first row) and after undergoing HIP treatment (second row). The first column provides a cross-sectional view of the sample generated with low AE(0.71 J/mm²)(a), revealing significant levels of LoFs. While the HIP process reduced porosity levels, complete closure of the pores was not achieved(d).

The second row showcases samples produced with moderate AE levels (1.07 J/mm²), displaying isolated and smaller-sized pores in the as-built condition(b). Consequently, these samples exhibited almost full density following HIP treatment (e). Finally, the third column represents samples created with sufficient AE(2.14 J/mm²), showcasing minimal levels of porosity characterized by small pore sizes. Notably, these samples displayed little to no visible changes post-HIP treatment, as they were inherently dense from the outset.

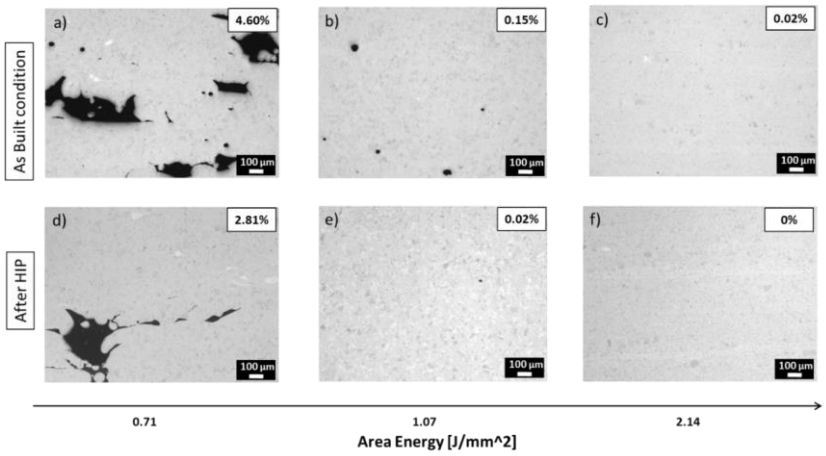


**Figure 41: Porosity vs Area Energy, for as built a), b), c) and after HIP samples d), e), f).**

Indeed, it is well-established that HIP treatment is only effective in closing pores that are already isolated and lack of fusions. Pores that are interconnected with the external surface cannot be consolidated through this process.

We used the visible border of open porosity as a guide to calculate the distance each wall needs to traverse to enter the region where HIP treatment can effectively close all instances of lack of fusion. To execute this, we conducted stitch imaging using an optical microscope on three selected candidates after the HIP treatment. This approach allowed us to gauge the extent to which HIP treatment could successfully address the lack of fusion issues by measuring the distance between the walls and the zone where the treatment is effective in closing these imperfections Figure 42.

This border analysis, which was later conducted, played a pivotal role in the design phase of our capsules' wall thickness.

Overall, this analysis allows to determine the position where the pores and lack of fusion can be consolidated by the HIP treatment. By understanding the critical distance at which HIP treatment becomes effective in closing lack of fusion issues, we could tailor the wall thickness of our capsules to ensure optimal densification outcomes in our samples. This strategic approach has been instrumental in achieving the desired material properties and the overall success of our study.

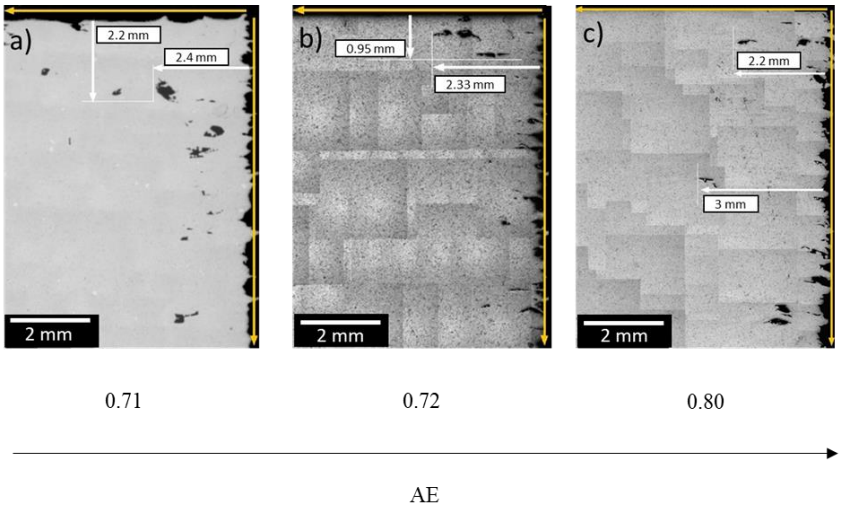


**Figure 42: Border analysis with stitched images for HIPed samples at different AE and porosity levels**

*Capsules*

Capsule samples measuring 18x18x18 mm were manufactured. In the production of these capsules, a distinct approach was employed. The outer segment, designated as the "wall" and measuring 3 mm in thickness, was produced using specific parameters geared toward achieving a high level of density. Conversely, the inner segment, referred to as the "core," was processed using lower-energy parameters, as outlined in Figure 43. The final design had a 1 mm overlapping region between the wall and the core to avoid detachment.

Furthermore, it is important to note that for each combination of process parameters detailed in Table 5, two capsules were manufactured. The production process involved employing a scanning strategy with a 90° rotation.

The pre-heating parameters were configured to achieve a temperature of approximately 1050 °C. Conversely, the melting parameters for the core section were selected to include fast beam speed, low beam current, and a large line offset. This choice was made to generate lower area energy and induce only limited densification while minimizing aluminium evaporation.

For this reason, the process parameters were selected to have a low area energy inferior to the area energy allowing the full melting and densification of the layer of powders, as reported in other works [96][97].

As shown in Figure 44, the as-built conditions in the first row clarifies the effect of such chosen process parameters on the level of porosity of the core. At the second row of the same figure, each condition is shown after being HIPed. Later, we will discuss the level of densification for each condition. The HIP treatment parameters were a temperature of 1260 °C, a pressure of 170 MPa, and a dwell time of 4 h, followed by furnace cooling.

Commented [GM2]: Here you can use like reference the work on
1)Wartbichler et al. On the formation Mechanism of Banded Microstructrues DOI: 10.1002/adem.202101199
2) Ghibaudo_
Influence of focus offset on the microstructure of an intermetallic γ-TiAl based alloy produced by electron beam powder bed fusion

Commented [GM3]: Instead of using a picture, i will create a real table with the parameters.

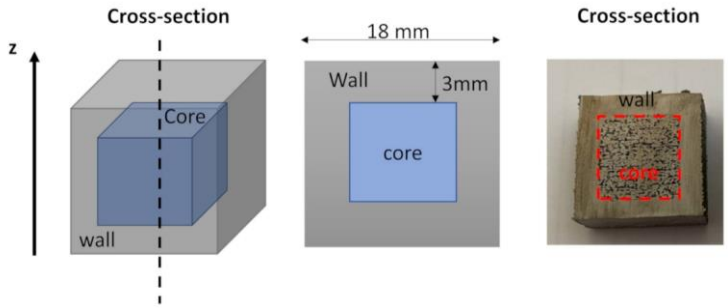


**Figure 43: Capsule design-Dens wall and low energy core.**

**Table 6: Process parameters employed for producing the capsule specimens. The constant parameters are the voltage of 60 kV, focus offset of 15 mA, and layer thickness of 90 µm with a scanning strategy of 90° rotation.**

| Samples | Beam Speed (mm/s) | Beam Current (mA) | Line Offset (mm) | Area Energy (J/mm²) |
|---|---|---|---|---|
| Wall part * | 1600 | 10 | 0.2 | 1.875 |
| Capsule-3000 | 3000 | 6 | 0.3 | 0.400 |
| Capsule-4000 | 4000 | 6 | 0.3 | 0.300 |
| Capsule-5000 | 5000 | 6 | 0.3 | 0.240 |
| Capsule-preheating | - | - | - | - |

**The same wall part parameters were used for all the capsules*

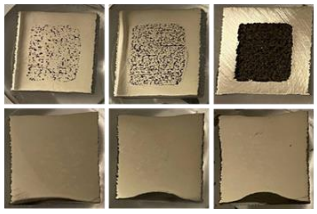


**Figure 44: Capsules in As Built-first row Condition vs After HIP-second row_**

**Beam spead from right to left: 3000, 4000, 5000(mm/s)_Beam current for all :6mA**

Commented [GM4]: Please reports also the scan speed

Figure 45 exhibit detailed LOM images of the capsule cross-sections at the core, both in the as-built and post-HIP conditions..The samples were fabricated with increasing beam speeds of 3000 mm/s, 4000 mm/s, and 5000 mm/s and beam current of 6 mA. Notably, the images illustrate that slower beam speeds, implying higher energy imparted to the powder, resulted in reduced porosity levels compared to the samples produced at faster scan rates.. This lower densification level can be attributed to the use of low-energy parameters, which were chosen to limit potential microstructure irregularities within the inner part of the capsules. It is worth noting that the residual porosity observed in the capsules subjected to inner pre-heating aligns with the findings of Bieske et al.[98], indicating consistency with prior research in this area. Following the HIP process, the LOM micrographs show fully densification for all the conditions.

Commented [GM5]: If you eliminate figures associated with beam current 8 mA you need to correct also the text and the order of the figures

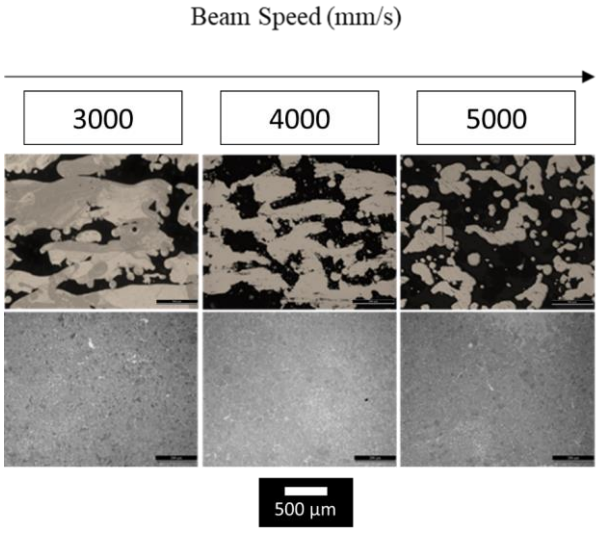


**Figure 45: Capsules cross-section in As-Built and after HIP Conditions _ Beam Current 6 mA.**

**Figure 46: Capsules cross-section in As-Built and after HIP Conditions _ Beam Current 8mA.**

Figure 47 illustrates the successful HIP densification for each condition in a concise manner. By overlaying overview images with LOM images from the core onto the graph depicting the level of porosity versus the beam speed, a clear trend for both as-built and post-HIP capsules is discernible. Notably, an increase in beam speed corresponds to higher porosity levels in the core of the capsules in the as-built condition, a trend that is also evident in the post-HIP conditions. At 3000 mm/s, the porosity exhibited values around 0.009%, demonstrating a remarkably low level of porosity. Increasing the beam speed to 4000 mm/s and 5000 mm/s, the porosity reached approximately 0.015% and 0.03%, respectively. Notably, the capsule produced solely with the pre-heating step in the core part displayed a slightly higher porosity level, hovering at around 0.09%. However, it is important to consider that, even with these slight variations in porosity, the overall residual porosity of the HIPed capsules remained exceptionally low.This outcome underscores the effectiveness of the HIP process in achieving the desired level of densification across a range of conditions, promising significant material quality for various applications.

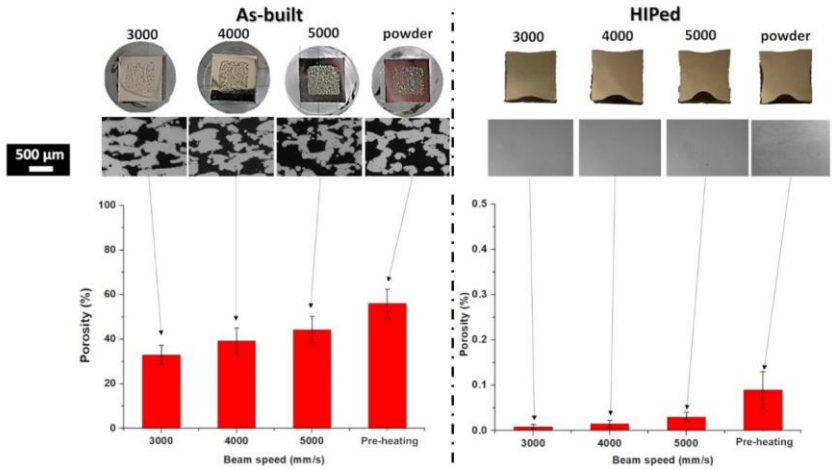


**Figure 47: Image, LOM images, and porosity level of the capsule samples processed using melting parameters with beam speed from 3000 to 5000 mm/s and only preheating parameters in the as-built and HIPed states** [99].

### 3.1.2 Deformation

The examination of HIPed capsules revealed a noticeable area shrinkage, primarily attributed to the consolidation of the inner part where the particles were only partially melted, as illustrated in Figure 48. It is important to note that this shrinkage factor exhibited an increasing trend with the acceleration of the electron beam speed, reaching its highest magnitude in the capsule produced without the melting step. The lowest recorded shrinkage stood at 6.6% for a beam speed of 3000 mm/s, while the highest recorded shrinkage soared to 20.7% for the capsule devoid of the melting step. These outcomes closely align with the level of porosity identified in the as-built capsules that increases with the increment of the beam speed. Therefore, the higher the porosity level, the more pronounced the shrinkage observed during the HIP treatment.

For a more in-depth analysis, a comparison was made between the capsules produced at a beam speed of 3000 mm/s (referred to as capsule-3000) and those produced without an inner melting step (referred to as preheating). This comparison is vital in designing components, as understanding area shrinkage post-HIP is crucial for accurate dimensioning. Notably, the results indicated that the capsule-3000 configuration mitigates the overestimation of part dimensions in their as-built state compared to the capsule-preheating.

It is worth mentioning that the distortion was not uniform on all sides of the capsule. The side attached to the building platform exhibited a slightly reduced thickness (approximately 2.8 mm instead of 3 mm) due to its interaction with the platform. Consequently, the shrinkage effect was more pronounced along that particular side. This is why the evaluation of area shrinkage, which considers the overall deformation of the components, was deemed more

pertinent. The implications of these findings are substantial. Ensuring a homogeneous thickness for the capsule borders is essential to eliminate preferential distortions that may occur on the thinner sides.

Furthermore, optimizing the thickness of the capsule borders is crucial. Excessively thin borders may harbor superficial defects reaching the inner part, which could promote argon flow during HIP treatment and hinder capsule densification. Conversely, excessively thick borders could lead to material overuse. Finally, the external wall could be removed by machining.

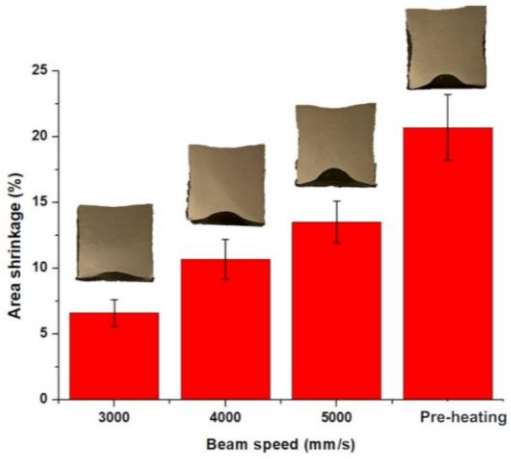


**Figure 48: Area shrinkage of HIPed capsules processed using different process parameters**[99]**.**

### 3.1.3 Microstructure

*Microstructure analyses*

To assess the microstructure comparison, we compared the core of the capsules after desification by HIP to massive samples produced using the parameters applied to the wall segment. Different focus offset settings of 10 mA and 30 mA were employed. The focus offset has a direct impact on the spot size of the electron beam, with the 10 mA setting resulting in a narrower spot size compared to the 30 mA setting, as reported in a previous work [96].

Figure 49 provides a comparative analysis of the LOM images captured from the cores of two capsules, alongside those of two mentioned massive samples, all post-HIP treatment. The HIPed capsules are compared to HIPed massive samples generated using different focus offset parameters, specifically 10 mA and 30 mA. In detail, Figure 49a displays the core of the capsule with pre-heating, while Figure 49b showcases the capsule at 3000 mm/s. In the second row, we observe Figure 49c, which represents the massive sample with a focus offset of 10 mA, and finally, Figure 49d represents the massive sample with a focus offset of 30 mA.

The samples produced with a focus offset of 10 mA (Figure 49c) exhibit a banded microstructure, indicating significant aluminum evaporation. In contrast, the samples fabricated with a focus offset of 30 mA (Figure 49) reveal a uniform microstructure without banded structures, suggesting minimal aluminum loss attributed to the melting step. This variation in microstructure is attributed to the different spot sizes of the electron beam, which influence the size of the melt pool. The smaller spot size corresponding to a focus offset of 10 mA results in a deeper and narrower melt pool, exacerbating aluminum evaporation. Conversely, the focus offset of 30 mA yields a larger spot size, creating a shallower and broader melt pool that mitigates aluminum evaporation. This observation underscores our success in producing capsules with a homogeneous microstructure and the absence of banded structures. However, a significant presence of PPBs was observed in the HIPed capsule-powder, particularly in the HIPed capsule-3000, which exhibited a moderate quantity of PPBs. These observations shed light on microstructural variations influenced by distinct processing parameters, offering critical insights for optimizing manufacturing processes and achieving desired material properties.

Moreover, Figure 49 presents the microstructure of the HIPed capsule-3000 sample, involving low-energy melting parameters. This configuration effectively limits the occurrence of PPBs compared to the previous example, displaying α2 phases characterized by smaller dimensions and a more uniform distribution throughout the material. Conversely, the HIPed capsule with pre-heating  Figure 49 exhibits more distinct PPBs and larger α2 phases, while the HIPed capsule-3000  Figure 49 manifests reduced PPBs and a more even distribution of smaller α2 phases. This understanding serves as a cornerstone for comprehending the influence of processing conditions on the internal attributes of the material, subsequently guiding the optimization of manufacturing processes to achieve the intended material properties. This will be discussed more in detail in the next figure.

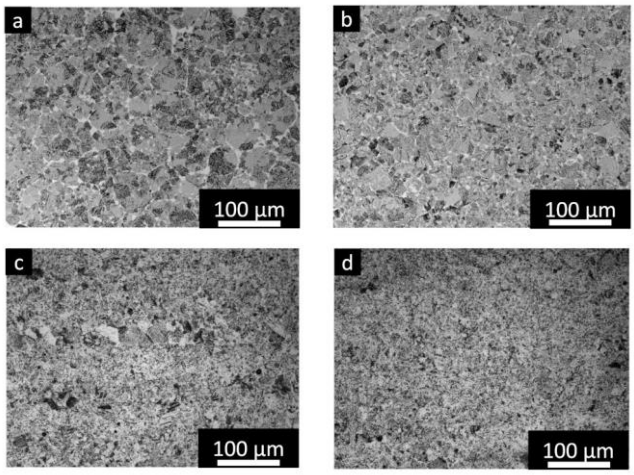


**Figure 49: . LOM images of HIPed TiAl samples: (a) capsule-pre-heatingpowder; (b) capsule-3000; (c) massive sample with a focus offset of 10 mA; (d) massive sample with a focus offset 30 mA.**

Further analysis (Figure 52) confirms our findings, as evident in the examination of capsule-powder. This analysis corroborates earlier research, indicating the formation of PPBs in HIPed capsules—a phenomenon attributed to aluminum (Al) evaporation during the pre-heating phase, notably at the powder particle surface. To enhance the manufacturing process, meticulous tailoring of the pre-heating step is essential to mitigate Al evaporation, aligning with prior studies. It is noteworthy that PPBs in this context differ from traditional HIPed TiAl powder in powder metallurgy, where surface oxygen enrichment typically stabilizes α2 phase formation under heat treatment. However, the formation of PPBs tends to be detrimental to mechanical properties, diminishing ductility and mechanical performance at elevated temperatures. Therefore, a concerted effort must be made to suppress their formation to ensure robust mechanical performance [100]. In the comprehensive assessment of microstructures, it is evident that the HIPed capsule-preheating and the HIPed capsule-3000 exhibit distinct characteristics in terms of grain sizes and phase distributions, as elaborated upon below:

The HIPed capsule-powder showcases γ grains spanning a range from 70 to 10 µm, with an average grain size of approximately 60 µm (Figure 50a). Conversely, the HIPed capsule-3000 presents γ grains within dimensions ranging from 50 to 6 µm, featuring an average grain size of approximately 44 µm (Figure 50).

Turning our attention to the α2 phase, the HIPed capsule-powder presents sizes ranging from a few microns up to around 30 µm, with an average size of about 23 µm (Figure 50a). On the other hand, the HIPed capsule-3000 sample exhibits α2 phase sizes ranging from a few microns to 25 µm, accompanied by an average size of approximately 13 µm (Figure 50b).

It is noteworthy that the internal core of the capsule underwent melting with low-energy parameters, followed by HIP treatment, resulting in smaller grains and a lower concentration of PPBs. This observation is strongly corroborated by the SEM+EDS scan line, which unequivocally confirms that the bright phase corresponds to the α2 phase. This is primarily due to the enrichment of titanium (Ti) and the depletion of aluminum (Al) (Figure 50).

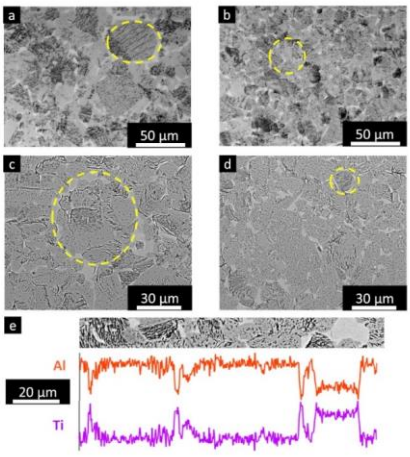


**Figure 50: . LOM images at high magnification of HIPed samples : (a) capsule-pre-heating; (b) capsule-3000; SEM image of (c) capsule-pre-heating; (d) capsule-3000; (e) SEM+EDS scan line showing that the bright phases are α2 phase enriched in Ti and depleted of Al; Some PPBs are pointed out by yellow circles in the LOM and SEM images.**

*Phase identification by EBSD analysis*

The EBSD maps of the HIPed capsule prehating and HIPed capsule-3000 are reported in Figure 51a Figure 51b, respectively. The HIPed capsule-pre-heating shows larger and higher frequency of α2 phase concentration, quantified at 5.7 ± 1.2%. Conversely, the HIPed capsule-3000 presents a more modest α2 phase concentration around 3.5 ± 0.3%.

Taking into consideration the TiAl phase diagram, it is imperative to note that the HIP treatment temperature applied (1260 °C) falls within the α+γ phase region, situated below the alpha transus temperature. However, due to the phenomenon of Al evaporation, the phase diagram is effectively shifted to a zone characterized by a higher quantity of α2 phase, maintaining the same temperature conditions. This critical insight underscores the complex interplay of temperature, phase transformations, and elemental compositions within the material, lending deeper comprehension to the microstructural nuances observed.

The thorough examination of grain sizes, phase distributions, and PPB concentrations between the HIPed capsule-powder and the HIPed capsule-3000 provides critical insights into the interplay of processing parameters and resulting microstructures. These findings offer a profound understanding of the material's internal characteristics, laying the foundation for precise control and optimization of manufacturing processes to achieve desired material properties.

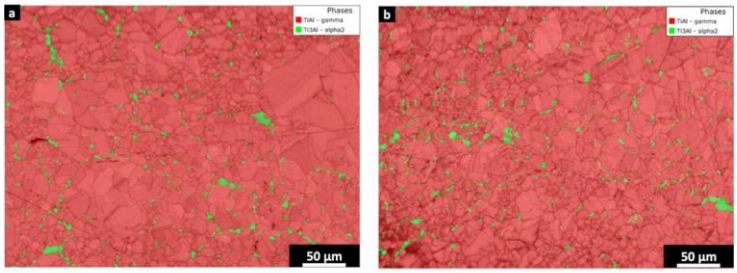


**Figure 51: EBSD phase map of (a) HIPed capsule-pre-heating powder and (b) HIPed capsule-3000. The red represents the γ-TiAl phase, while the green indicates the α2 phase. Some PPBs are pointed out by yellow circles in the EBSD maps.**

### 3.1.4 Al evaporation

Figure 52 shows the trend of Al evaporation for the capsule samples and massive FO samples produced with focus offset of 10 mA and 30 mA after HIP treatment. The capsule-pre-heating exhibited the highest Al content due to limited Al depletion during the pre-heating step. Conversely, the increment of the area energy obtained by the melting step gradually involved the Al evaporation from beam speed of 5000 mm/s to 3000 mm/s. These results confirmed that the capsule approach allowed to produce samples with more mitigated Al evaporation with respect to the massive samples produced with focus offsets of 30 mA and 10 mA.

Reducing beam speed increased energy density on the powder, enlarging the melt pool and causing more Al evaporation. In contrast, low-energy melting parameters resulted in less Al-loss compared to massive sample production. This approach holds promise in mitigating issues seen in massive samples, such as layered microstructures due to significant Al-loss at the top of the melt pool.

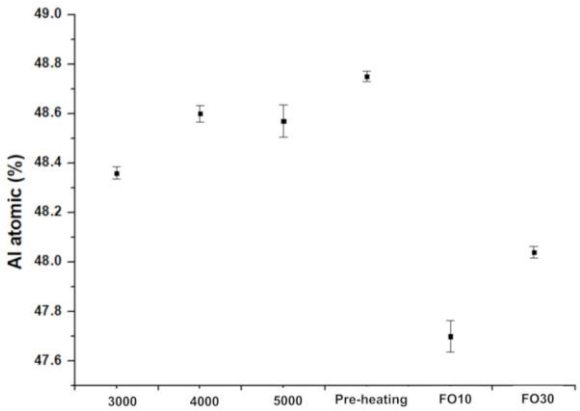


**Figure 52: . Al atomic percentage of the capsules and massive samples produced with different parameters by XRF analysis** [99].

### 3.1.5 XRD investigation

In the current microstructural analysis, specifically shown in Figure 50, it becomes evident that small PPBs remain detectable in the HIPed capsule-3000 samples, while the suppression of larger PPBs appears to be facilitated by the application of the melting step. This suggests that smaller particles experience a more pronounced loss of aluminum (Al) content during the pre-heating step, possibly due to their higher surface-to-volume ratio.

X-ray diffraction (XRD) analysis was conducted on the powder, categorizing it into three size groups: small (< 53 µm), medium (53 to 106 µm), and large (> 106 µm). The XRD results (Figure 53) demonstrated an interesting trend. Small particles exhibited the highest concentration of the α2 phase, indicative of increased Al depletion, while medium-sized particles displayed a lower quantity of the α2 phase. Finally, the largest particles did not show any apparent presence of the α2 phase.

This observation suggests that particle size plays a crucial role in the extent of Al loss during the pre-heating step. However, it emphasizes fine-tuning pre-heating parameters to minimize surface Al-loss, particularly for smaller particles. In terms of the implications for powder recycling, it becomes evident that recycling powder with a higher α2 fraction, typically associated with smaller particles, may heighten the risk of PPB formation. This concern becomes particularly relevant when employing the EB-PBF capsule production method alongside HIP treatment to achieve dense samples.

In contrast, when producing massive samples using standard melting parameters, the risk of PPB formation diminishes considerably, primarily due to the complete melting of particles. These findings underscore the complexities of powder behavior during processing and carry significant implications for optimizing manufacturing processes to attain desired material properties while minimizing the risk of PPB-related issues.

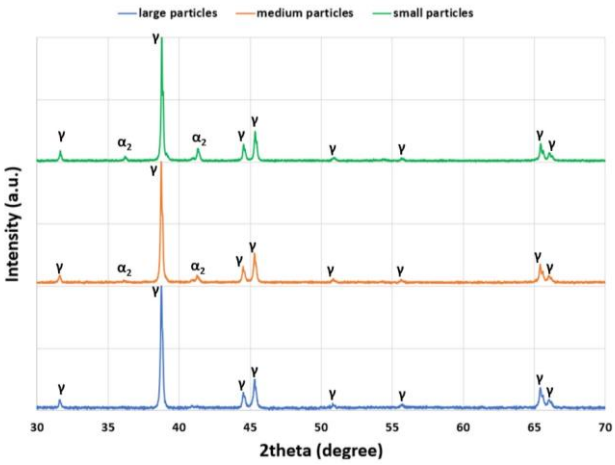


**Figure 53: XRD patterns of the powder in three different particle size distributions: small particles (< 53 µm), medium particles (from 53 to 106 µm), and large particles (> 106 µm)** [99].

## 3.2 Ti6Al4V Produced by L-PBF

In this chapter, the investigation explores HIP's role in defect remediation, particularly targeting keyhole porosities and lack of fusion, and their impacts on the microstructure of Ti64 components produced via LPBF. Initial experiments applied standard HIP parameters—920°C, 150 MPa, and a 2-hour dwell (120 minutes)—across a wide range of VE values as shown in [101][102][103]. Porosity assessments were conducted on both as-built and HIP-treated samples under identical processing conditions.

**Table 7: Process parameters employed for producing the massive Ti64 specimens.**

| Sample | Laser Power (W) | Beam Speed (mm/s) | VED |
|---|---|---|---|
| 1 | 100 | 1300 | 12.82 |
| 2 | 100 | 1050 | 15.87 |
| 3 | 100 | 900 | 18.52 |
| 4 | 250 | 1490 | 27.96 |
| 5 | 75 | 372 | 33.60 |
| 6 | 75 | 319 | 39.18 |
| 7 | 200 | 600 | 55.56 |
| 8 | 175 | 474 | 61.00 |
| 9 | 200 | 450 | 74.07 |

Further analyses evaluated reduced HIP durations to identify opportunities for densifying samples with shorter post-processing times, specifically examining 30-minute, 10-minute, and 3-minute dwell times to observe microstructural changes. Understanding HIP kinetics and its effect on Ti64 microstructure is critical for elucidating the mechanisms driving defect healing and enhancement of material properties. The research also investigates how capsule geometry, particularly wall thickness and size, influences deformation or shrinkage during HIP. Capsules with varied geometries were designed to examine deformation patterns, aiming to optimize the additive manufacturing process, minimize defects, and improve efficiency. This insight is pivotal for developing strategies for capsule design that either shorten production times or achieve targeted microstructural characteristics through HIP with minimal or controlled deformation.

The evaluation of these objectives encompassed a three-step experimental analysis: Porosity, Microstructure, and Deformation.

### 3.2.1 Massive samples

*Porosity*

In Figure 54, the classification of as-built samples into three VED-based groups reveals distinct responses to HIP treatment. The first group, characterized by low VED, shows a high incidence of LOF due to inadequate energy application, leading to significant and interconnected defects that extend to the sample's surface. These characteristics challenge HIP's effectiveness in defect remediation due to the defects' open and surface-connected nature[104]. However, within this same group, an increase to VED=25.64 J/mm³ marks a critical transition where LOF defects become more isolated and less surface-connected, significantly improving HIP's ability to densify these components. Notably, 30-minute, 10-minute, and even 3-minute HIP treatment can nearly fully densify samples at this VED, highlighting its potential for efficient densification. The sample with VED=25.64 J/mm³, exhibiting isolated LOF in its as-built condition and achieving full density after all HIP durations, was selected for in-depth microstructural analysis. This choice is based on its status as the lowest VED condition that was fully densified by HIP, indicating that samples can be manufactured with reduced energy yet still be effectively densified through HIP.

The second group falls within an optimal VED range, producing samples that are already highly dense. HIP treatment in this scenario shows minimal impact, suggesting that initial LPBF settings were effectively optimized to achieve optimal density without needing HIP.

Lastly, the third group, with high VED, develops keyhole porosity due to excessive energy input during LPBF. Unlike the LOF seen in the low VED group, these defects are isolated and closed, making them suitable candidates for HIP treatment. The effectiveness of both 2-hour and 30-minute HIP treatments for this group demonstrates HIP's adaptability in correcting defects induced by varying VED conditions, showcasing its broad applicability in additive manufacturing defect remediation.

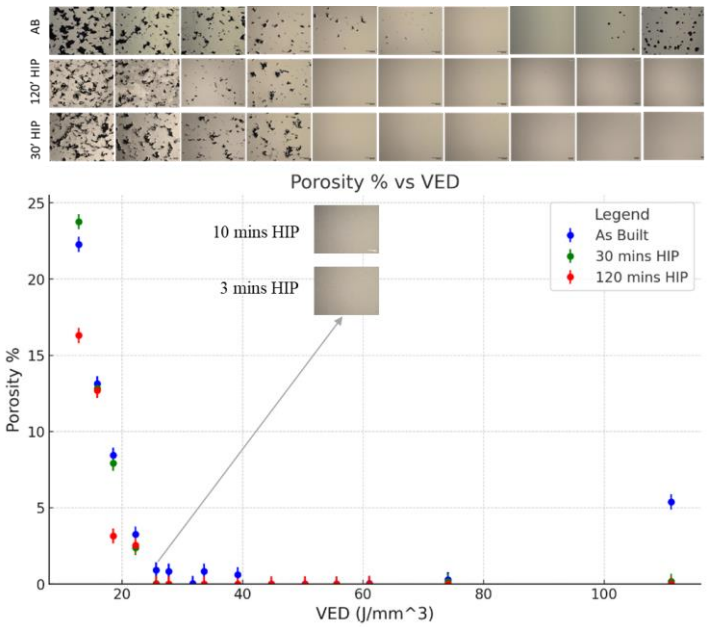


**Figure 54: Porosity level in AB, Standard HIP and 30 mins HIP vs VED**

*Border analysis*

The border analysis shown in Figure 55 aimed to distinguish between the zones of the sample affected by HIP and those left unchanged due to the proximity of the surface. the measured distances were uniformly small, leading to the general observation that, except for porosities very close to the surface, HIP successfully densified all other LOFs.In the second row of the analysis, an overview is provided, showing the sample in its as-built condition alongside its state after undergoing various HIP treatments. This comparative perspective aims to visually document the effectiveness of HIP in modifying the sample's microstructure, offering insights into how different treatment durations impact the densification process and the overall integrity of the sample. This visual documentation serves as a crucial tool for understanding the transformative effects of HIP on addressing defects and enhancing material properties, particularly in highlighting the technique's capability to consolidate areas previously compromised by LOFs, barring those immediately adjacent to the sample's surface.

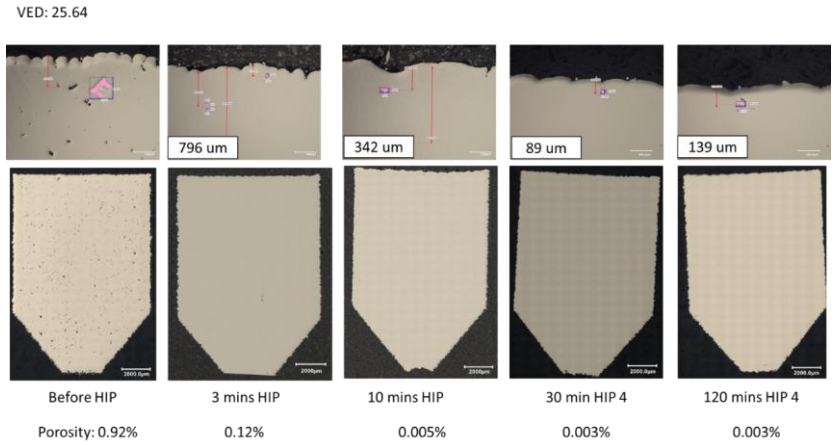


**Figure 55: Border analysis performed on the as-built and HIPed samples**

*Microstructure*

The impact of HIP on the microstructure of Ti64 is pivotal, especially considering how varying durations of HIP treatments, including 120-minute, 30-minute, 10-minute, and even 3-minute sessions, affect grain structure, phase composition, and texture. Utilizing XRD and EBSD, our study delves into the microstructural transformations induced by these different HIP durations on Ti64. The XRD analysis sheds light on crystallographic structure changes, offering insights into phase shifts and texture modifications. Simultaneously, EBSD provides a granular view of the adjustments in grain boundaries, orientations, and the extent of recrystallization phenomena, which are crucial in understanding the HIP process's efficacy. This multifaceted approach, combining XRD and EBSD, facilitates a comprehensive understanding of how short and conventional HIP durations contribute to microstructural evolution and influence the mechanical properties of Ti64.

XRD

As shown in

Figure 56, the XRD pattern analysis for Ti64, produced via SLM and subsequently treated with HIP, reveals critical information about the microstructural evolution across different HIP durations. Initially, the as-printed cross-section sample predominantly exhibits α phase peaks, with a notable absence of a β phase peak around 39.5 degrees 2θ. As HIP treatment progresses

from 3 to 120 minutes, not only does the β phase peak emerge, but it also sharpens and intensifies. This trend signifies an increase in the β phase's presence within the microstructure, likely due to the diffusion of vanadium, which serves as a β stabilizer in Ti64, and the relaxation of the material under the thermal conditions of HIP [105].The increased sharpness and intensity of the β phase peak with extended HIP durations suggest a decrease in peak broadening, a phenomenon often attributed to factors such as crystal size and inhomogeneous strain. A sharpened peak typically indicates larger crystal size and reduced strain, implying that the HIP process may be promoting crystal growth and homogenization of the microstructure. Conversely, broader peaks could suggest smaller crystal sizes and greater strain within the material[106][107].The simultaneous determination of mean crystal size and strain from the XRD pattern is a complex endeavor that has challenged powder diffractionists. However, applying both approximate and more rigorous analytical methods to our cross-sectional samples, it is inferred that the observed variations in peak width, intensity, and sharpness are indicative of changes in crystal size and strain levels. Hence, the XRD patterns suggest that HIP treatment not only contributes to the stabilization of the β phase but also enhances the quality of the microstructure, with a reduction in defects and inhomogeneities, affirming HIP's role in refining the mechanical properties of SLM-produced Ti64 components [108][109].

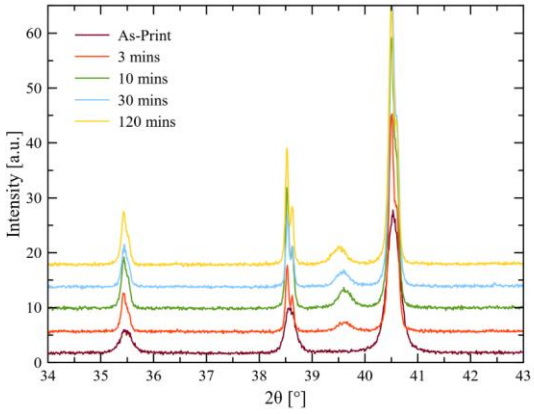


**Figure 56: XRD pattern for Ti64 samples in the as-built condition and after HIP treatment for 120 mins,30 mins,10 mins and 3 mins.**

The c/a ratio, indicative of the hexagonal close-packed (hcp) structure's axial dimensions in Ti64, is a crucial parameter for assessing microstructural characteristics. An equilibrium c/a ratio reflects a balance between the lattice parameters 'c' and 'a', signifying minimal internal stresses and a stable α phase[110]. The provided graph in Figure 57 post-SLM production reveals an initial c/a ratio slightly above this equilibrium value for the as-built condition, suggesting a state of residual stress or a non-equilibrium phase. HIP treatment initiates a rapid

decrease in this ratio within the first 3 minutes, indicating stress relief and a move toward equilibrium. Subsequent HIP durations up to 120 minutes show the c/a ratio approaching and stabilizing near the equilibrium value for α-Ti64, underscoring the HIP process's effectiveness in homogenizing and stabilizing the microstructure of Ti64 post-manufacturing.

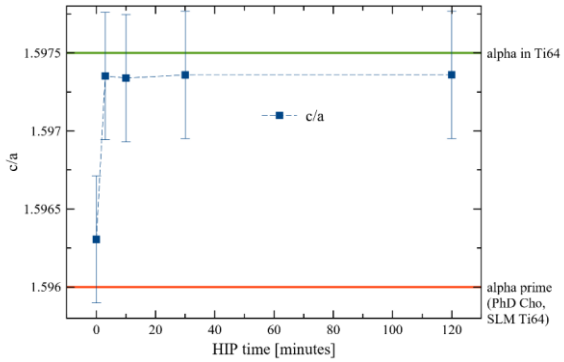


**Figure 57: Evolution of c/a Ratio in Ti64 Microstructure Post-SLM and HIP Treatment**[110]

EBSD

The EBSD analysis of the as-built Ti64 samples, as illustrated in Figure 58, unveils a microstructure typified by diverse grain sizes and irregular grain boundaries, emblematic of the anisotropic and heterogeneous nature intrinsic to as-built L-PBF materials. The columnar grains, extending along the build direction, stand out prominently in the as-built sample, underscoring the directional solidification patterns during fabrication. Post the 120-minute HIP treatment, the EBSD images capture a remarkable microstructural refinement: grain distributions appear more homogeneous, and there is a conspicuous decrement in the density of grain boundaries (dark boundaries). This evolution signifies a considerable grain growth or coarsening, and the microstructure's orientation refines to a point where the initial build direction influence becomes obscured. Contrastingly, the 30-minute HIP treatment delineates an intermediate state of microstructural refinement. Although there is a discernible reduction in grain boundary density and a movement towards a more equiaxed grain structure, it is less marked than the 2-hour HIP sample. This suggests a more moderate enhancement in grain growth and crystalline orientation, with some retention of the as-built microstructural characteristics. Collectively, these EBSD images chronicle the microstructural progression from the as-fabricated state through successive HIP treatments, highlighting the direct correlation between HIP duration and the resulting grain structure and orientation within the Ti64 alloy.

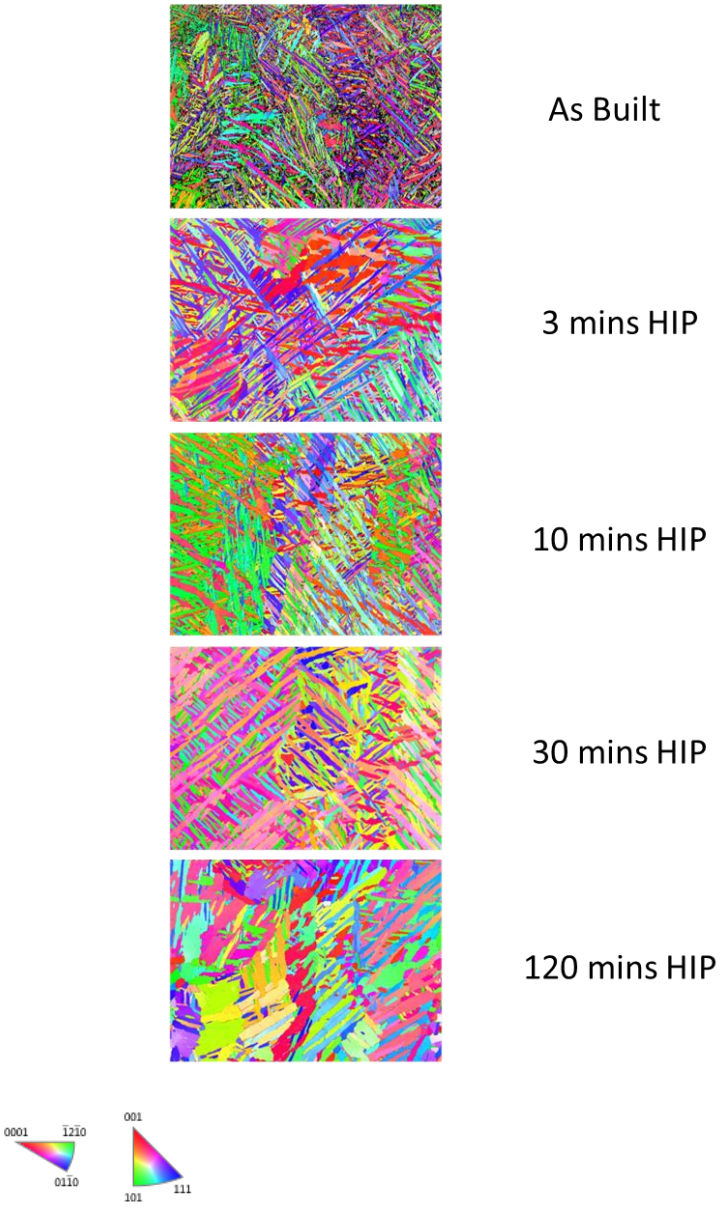


**Figure 58: EBSD results for As Built , 3 mins HIP, 10 mins HIP, 30 mins HIP, and 120 mins HIP Ti64 samples**

Commented [GM6]: Please add the IPF map

Figure 59 showss the EBSD phase mapping across the Ti64 samples, as depicted in the sequence of images from the as-built state to extended HIP durations, and illustrates the phase evolution within the material. In the as-built condition, the image is saturated with the red phase, indicative of a dominant alpha-titanium microstructure, interspersed with minor instances of secondary phases as evidenced by the sporadic specks of alternative colors. The dominance of the alpha phase is characteristic of the microstructural state post-manufacturing, yet the presence of other phases, albeit minimal, alludes to the potential for phase diversity within the as-built material.

Progressing to the 3-minute HIP treatment, there is a noticeable decrease in the secondary phase content, which can be inferred from the reduction of non-red speckling. This suggests the onset of phase homogenization, possibly due to the diffusion processes initiated by the HIP cycle. As the HIP time extends to 10 minutes, the phase distribution appears marginally more homogeneous compared to the 3-minute condition, yet still contains a significant amount of secondary phases. This implies that while phase transformation is occurring, it does not reach completion within this timeframe.

The 30-minute HIP image reveals a further reduction in secondary phases, with the red alpha-titanium matrix becoming more pronounced and the secondary phases receding. The continued HIP treatment for 120 minutes culminates in a microstructure where the alpha phase is overwhelmingly predominant, with the other phases now reduced to a mere trace. The almost uniform red phase coloration illustrates a microstructure that has undergone substantial phase transformation, aligning the material composition towards a more stable and uniform alpha phase distribution. This evolution of the phase landscape underscores the effectiveness of HIP treatment in promoting phase stability and uniformity, a critical factor in enhancing the material's overall properties and performance.

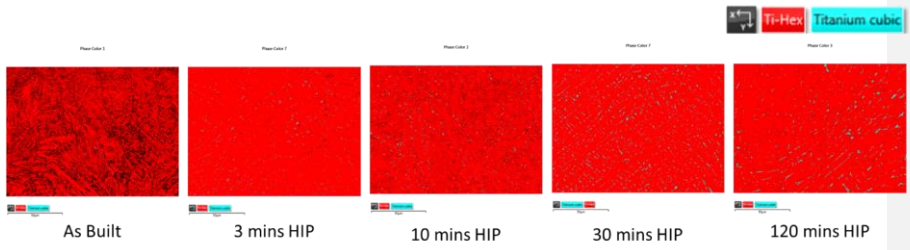


**Figure 59: EBSD-Phase mapping results for As Built , 3 mins HIP, 10 mins HIP, 30 mins HIP, and 120 mins HIP Ti64 samples**

### 3.2.2 Capsules

*Design of Capsule for Deformation Control*

At this stage, the study focused on investigating HIP-induced deformations in Ti64 capsules containing loose powder. As shown in Figure 60, two distinct groups of capsules were meticulously designed to assess the influence of varying geometric parameters on the deformation process. The process parameter used is the standard set of process parameters for producing dense and deffection-free Ti64 samples with L-PBF machine of use (VED=55 J/mm$^3$ ). The first group comprised cubic samples with consistent wall thickness and three different sizes (a), enabling the examination of the impact of size differentials on deformation behavior. In contrast, the second group (b) consisted of capsules with identical dimensions but varying wall thicknesses, facilitating an in-depth analysis of the role of wall thickness in influencing the deformation patterns. The intricate design of these capsule groups laid the foundation for comprehensively evaluating the effects of HIP treatment on the solidification of loose powder within the cubic samples.

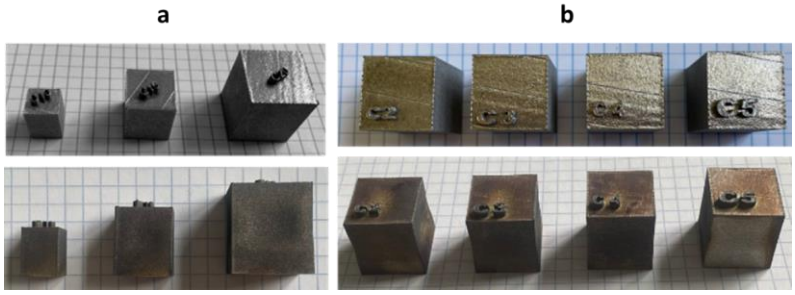


**Figure 60: Two groups of Designed Capsules before and after HIP: a) Capsules varying in size with fixed wall thickness, b) Capsules fixed in size with varying wall thickness**

*HIP-Induced Solidification and Deformation Analysis by Cross-Section Image Analysis*

The HIP-induced deformation study on Ti64 capsules encapsulating loose powder reveals a tangible interplay between geometric dimensions and resultant structural integrity. Employing a mathematical model where deformation is a function of the powder to capsule volume ratio, a clear trend emerges: capsules with a constant wall thickness exhibit a linear deformation increase with the volume ratio, whereas variable wall thickness capsules demonstrate a quadratic surge as shown in Figure 61. This disparity underscores the substantial influence of wall thickness on withstanding HIP-induced internal stresses. Notably, the deformation is expressed as

$$\boldsymbol{D = axR^2 + bxR + c}$$

with the volume ratio R being calculated as

$$R = \left(\frac{a - 2w}{a}\right)^3$$

Figure 61 shows that the smallest capsules, with their superior wall-to-volume ratio, maintain their form more effectively under HIP conditions, while the larger counterparts succumb to greater deformation. Simultaneously, capsules with thinner walls display more pronounced deformation despite uniform external dimensions, reinforcing the notion that material distribution within the capsule's architecture is paramount to mitigating HIP-related distortions. This analytical approach, grounded in empirical evidence, provides a robust framework for predicting deformation behaviors in HIP-processed Ti64 capsules, facilitating the optimization of design parameters for enhanced dimensional stability. While the current trend observed lays a foundational understanding, the accuracy of the deformation prediction model is expected to improve with the addition of more data points. Nonetheless, these initial results can serve as a valuable stepping stone for future work, offering preliminary design suggestions for developing more resilient capsule geometries in HIP applications.

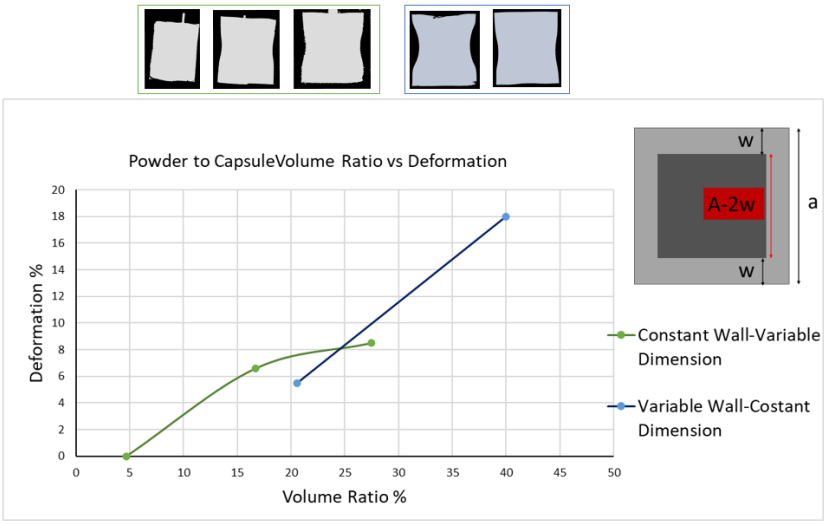


**Figure 61: Deformation- Ratio trend**

# Conclusion

The comprehensive exploration of Ti6Al4V and TiAl alloys through L-PBF and EB-PBF processes , followed by HIP, has marked a significant advancement in the understanding of additive manufacturing and post-processing treatments. This thesis meticulously investigated the microstructural evolution and the effects of HIP on defect remediation within these critical aerospace and biomedical alloys, offering new insights into the optimization of manufacturing processes for enhanced material performance.

For TiAl alloys, the focus on intermetallic γ-titanium aluminide (TiAl) underscores its potential for high-temperature applications due to its favorable properties such as low density, high specific strength, and excellent resistance to oxidation and creep deformation. The adoption of EB-PBF in manufacturing TiAl components represents a paradigm shift towards creating complex geometries while minimizing aluminum evaporation, a recurring challenge that affects microstructural uniformity and mechanical integrity. This thesis highlighted the strategic manipulation of process parameters to counteract aluminum loss, thereby promoting densification and achieving a homogeneous microstructure conducive to high-performance applications. The magnitude of aluminum loss is closely correlated with the process parameters, with highly energetic settings causing significant evaporation. This loss leads to different microstructures, including the formation of inhomogeneous banded structures, which negatively impact mechanical performance. To address this, the current work focused on creating EB-PBFed TiAl capsules using a pre-heating step and low-energy melting parameters, applying high beam speeds ranging from 5000 to 3000 mm/s. This approach aimed to reduce aluminum loss and microstructural inhomogeneity after hot isostatic pressing (HIP). The results demonstrated that the HIP treatment effectively densified the capsules, achieving a relative density of around 100%. Additionally, aluminum loss was significantly limited, as determined by X-ray fluorescence (XRF) analysis. Capsules produced with the pre-heating step showed an atomic percentage of aluminum of 48.75%, while those produced with low-energy melting parameters had 48.36%. In contrast, samples produced with standard, more energetic parameters showed lower atomic percentages, ranging from 48.04% to 47.70%. Future works can be related to study alternative preheating parameters or alternative melting parameters to reduce the presence of PPBs particles and at the same time mitigate the Al loss to obtain an homogenous microstructure.

In parallel, the comprehensive study on Ti6Al4V has unraveled the critical role of HIP in enhancing the material's microstructure and mechanical properties. Through detailed porosity analysis, deformation studies, and advanced microstructural characterization, this work has established a predictive model for optimizing the L-PBF process parameters and HIP conditions. This model not only facilitates the production of near-full density components but also guides the design of capsules to control deformation effectively, thereby ensuring the structural integrity of encapsulated materials.

The classification of as-built samples into VED-based groups revealed distinct HIP responses, with optimal VED conditions enabling near-complete densification even with short HIP durations. XRD and EBSD analyses highlighted significant microstructural transformations, including increased β phase presence, grain refinement, and phase homogenization, particularly notable at HIP durations ranging from 3 to 120 minutes. These findings validate the predictive model, demonstrating HIP's efficacy in enhancing density, phase stability, and mechanical properties, thereby confirming its crucial role in refining L-PBF-produced Ti6Al4V components.

The thesis has contributed to the additive manufacturing field by elucidating the complex interplay between additive manufacturing process parameters, HIP treatment, and the resultant material characteristics. The insights gained from this research not only enhance the current understanding of Ti6Al4V and TiAl alloys but also lay a solid foundation for future studies aimed at refining additive manufacturing techniques and post-processing treatments. As we stand on the cusp of a new era in materials engineering, this work underscores the importance of continued exploration and innovation in additive manufacturing, promising to unlock new possibilities in material science and engineering.

The methodologies developed and the knowledge acquired hold the potential to revolutionize manufacturing practices, steering the industry towards more efficient, sustainable, and high-quality production methods. The journey of discovery and innovation in the realm of additive manufacturing and HIP processing is far from over, with each new finding propelling us toward a future where the boundaries of material performance are continually expanded. Although this method shows significant improvement in the microstructure of the alloys, it would be beneficial for future research to complement these findings with a comprehensive set of mechanical property tests. This additional step would provide a more complete validation of the positive outcomes, ensuring that the enhanced microstructure translates into superior mechanical performance.

Commented [GM7]: Ok,. This is the added part

As innovation continues to drive the field forward, the potential for groundbreaking advancements in material science and engineering remains vast, heralding an exciting future for additive manufacturing.

# References

[1] D. R. Eyers and A. T. Potter, “Industrial Additive Manufacturing: A manufacturing systems perspective,” *Comput. Ind.*, vol. 92–93, pp. 208–218, 2017, doi: 10.1016/j.compind.2017.08.002.

[2] T. Duda and L. V. Raghavan, “3D metal printing technology: the need to re-invent design practice,” *AI Soc.*, vol. 33, no. 2, pp. 241–252, 2018, doi: 10.1007/s00146-018-0809-9.

[3] S. M. Yusuf, S. Cutler, and N. Gao, “Review : The Impact of Metal Additive Manufacturing on the Aerospace Industry,” 2019, doi: 10.3390/met9121286.

[4] A. Kirchheim, H. Dennig, and L. Zumofen, “Why Education and Training in the Field of Additive Manufacturing is a Necessity Why Education and Training in the Field of Additive Manufacturing is a Necessity The Right Way to Teach Students and Professionals,” no. December 2017, 2018, doi: 10.1007/978-3-319-66866-6.

[5] S. Rouf *et al.*, “Additive manufacturing technologies : Industrial and medical applications,” vol. 3, no. January, pp. 258–274, 2022, doi: 10.1016/j.susoc.2022.05.001.

[6] M. Attaran, “Additive Manufacturing: The Most Promising Technology to Alter the Supply Chain and Logistics,” *J. Serv. Sci. Manag.*, vol. 10, no. 03, pp. 189–206, 2017, doi: 10.4236/jssm.2017.103017.

[7] I. Gibson, D. Rosen, and B. Stucker, *（BOOK）Directed Energy Deposition Processes. In: Additive Manufacturing Technologies*. 2015.

[8] D. Godec, J. Gonzalez-gutierrez, A. Nordin, E. Pei, and J. Ureña, *A Guide to Additive Manufacturing*. 2022.

[9] I. Campbell, D. Bourell, and I. Gibson, “Additive manufacturing: rapid prototyping comes of age,” *Rapid Prototyp. J.*, vol. 18, no. 4, pp. 255–258, 2012, doi: 10.1108/13552541211231563.

[10] P. F. Egan, “Design for Additive Manufacturing: Recent Innovations and Future Directions,” *Designs*, vol. 7, no. 4, p. 83, 2023, doi: 10.3390/designs7040083.

[11] L. C. Zhang and H. Attar, “Selective Laser Melting of Titanium Alloys and Titanium Matrix Composites for Biomedical Applications: A Review,” *Adv. Eng. Mater.*, vol. 18, no. 4, pp. 463–475, 2016, doi: 10.1002/adem.201500419.

[12] T. Sik, J. Dongeung, K. Ginam, H. Chang, B. Yoon, and H. Do, “Powder based additive manufacturing for biomedical application of titanium and its alloys : a review,” *Biomed. Eng. Lett.*, vol. 10, no. 4, pp. 505–516, 2020, doi: 10.1007/s13534-020-00177-2.

[13] V. Juechter, M. M. Franke, T. Merenda, A. Stich, C. Körner, and R. F. Singer, “Additive manufacturing of Ti-45Al-4Nb-C by selective electron beam melting for automotive applications,” *Addit. Manuf.*, vol. 22, no. November 2017, pp. 118–126, 2018, doi: 10.1016/j.addma.2018.05.008.

[14] P. Ahangar, M. E. Cooke, M. H. Weber, and D. H. Rosenzweig, “applied sciences Current Biomedical Applications of 3D Printing and Additive Manufacturing,” 2019.

[15] L. E. Murr *et al.*, “Characterization of titanium aluminide alloy components fabricated by additive manufacturing using electron beam melting,” *Acta Mater.*, vol. 58, no. 5, pp. 1887–1894, 2010, doi: 10.1016/j.actamat.2009.11.032.

[16] B. Blakey-milner *et al.*, “Materials & Design Metal additive manufacturing in aerospace : A review,” *Mater. Des.*, vol. 209, p. 110008, 2021, doi: 10.1016/j.matdes.2021.110008.

[17] L. Meng *et al.*, “From Topology Optimization Design to Additive Manufacturing : Today ’ s Success and Tomorrow ’ s Roadmap,” *Arch. Comput. Methods Eng.*, vol. 27, no. 3, pp. 805–830, 2020, doi: 10.1007/s11831-019-09331-1.

[18] B. Hu *et al.*, “An Overview of Various Additive Manufacturing Technologies and Materials for Electrochemical Energy Conversion Applications,” 2022, doi: 10.1021/acsomega.2c05096.

[19] *Technical , Economic and Societal Effects of Manufacturing 4 . 0 Automation , Adaption and Manufacturing in Finland and Beyond*. .

[20] W. E. Frazier, “Metal additive manufacturing: A review,” *J. Mater. Eng. Perform.*, vol. 23, no. 6, pp. 1917–1928, 2014, doi: 10.1007/s11665-014-0958-z.

[21] T. Majumdar, T. Bazin, E. M. C. Ribeiro, J. E. Frith, and N. Birbilis, “Understanding the effects of PBF process parameter interplay on Ti-6Al-4V surface properties,” *PLoS One*, vol. 14, no. 8, pp. 1–24, 2019, doi: 10.1371/journal.pone.0221198.

[22] Y. Zhong *et al.*, “Additive manufacturing of ITER first wall panel parts by two approaches: Selective laser melting and electron beam melting,” *Fusion Eng. Des.*, vol. 116, pp. 24–33, 2017, doi: 10.1016/j.fusengdes.2017.01.032.

[23] M. L. Gatto *et al.*, “Topological, mechanical and biological properties of Ti6Al4V scaffolds for bone tissue regeneration fabricated with reused powders via electron beam melting,” *Materials (Basel).*, vol. 14, no. 1, pp. 1–20, 2021, doi: 10.3390/ma14010224.

[24] L. E. Murr *et al.*, “Metal Fabrication by Additive Manufacturing Using Laser and Electron Beam Melting Technologies,” *J. Mater. Sci. Technol.*, vol. 28, no. 1, pp. 1–14, 2012, doi: 10.1016/S1005-0302(12)60016-4.

[25] R. Lancaster, G. Davies, H. Illsley, and S. Jeffs, “Structural Integrity of an Electron Beam Melted Titanium Alloy,” no. May 2017, 2016, doi: 10.3390/ma9060470.

[26] V. Sonkamble and N. Phafat, “A current review on electron beam assisted additive manufacturing technology : recent trends and advances in materials design,” *Discov. Mech. Eng.*, 2023, doi: 10.1007/s44245-022-00008-x.

[27] C. Körner, “Additive manufacturing of metallic components by selective electron beam melting - A review,” *Int. Mater. Rev.*, vol. 61, no. 5, pp. 361–377, 2016, doi: 10.1080/09506608.2016.1176289.

[28] P. K. Gokuldoss, S. Kolla, and J. Eckert, “Additive Manufacturing Processes : Selective Laser Melting , Electron Beam Melting and Binder,” 2017, doi: 10.3390/ma10060672.

[29] M. Q. Zafar, “Finite element framework for electron beam melting process simulation,” pp. 2095–2112, 2020.

[30] N. Samiei, “Recent trends on applications of 3D printing technology on the design and manufacture of pharmaceutical oral formulation : a mini review,” vol. 4, 2020.

[31] L. E. Murr, “Metallurgy of additive manufacturing : Examples from electron beam melting,” *Addit. Manuf.*, vol. 5, pp. 40–53, 2015, doi: 10.1016/j.addma.2014.12.002.

[32] F. Calignano *et al.*, “Overview on additive manufacturing technologies,” *Proc. IEEE*, vol. 105, no. 4, pp. 593–612, 2017, doi: 10.1109/JPROC.2016.2625098.

[33] H. Lee, H. Kim, H. Hong, and B. Lee, “In fl uence of the focus offset on the defects , microstructure , and mechanical properties of an Inconel 718 superalloy fabricated by electron beam additive manufacturing,” *J. Alloys Compd.*, vol. 781, pp. 842–856, 2019, doi: 10.1016/j.jallcom.2018.12.070.

[34] J. Knörlein, M. M. Franke, M. Schloffer, and C. Körner, “In-situ aluminum control for titanium aluminide via electron beam powder bed fusion to realize a dual microstructure,” *Addit. Manuf.*, vol. 59, no. August, 2022, doi: 10.1016/j.addma.2022.103132.

[35] V. Lunetto, M. Galati, L. Settineri, and L. Iuliano, “Unit process energy consumption analysis and models for Electron Beam Melting (EBM): Effects of process and part designs,” *Addit. Manuf.*, vol. 33, no. February, p. 101115, 2020, doi: 10.1016/j.addma.2020.101115.

[36] E. M. Sefene, “State-of-the-art of selective laser melting process: A comprehensive review,” *J. Manuf. Syst.*, vol. 63, no. April, pp. 250–274, 2022, doi: 10.1016/j.jmsy.2022.04.002.

[37] C. L. Li *et al.*, “Realizing superior ductility of selective laser melted Ti-6Al-4V through a multi-step heat treatment,” *Mater. Sci. Eng. A*, vol. 799, no. October 2020, p. 140367, 2021, doi: 10.1016/j.msea.2020.140367.

[38] C. Y. Yap *et al.*, “Review of selective laser melting: Materials and applications,” vol. 041101, 2015, doi: 10.1063/1.4935926.

[39] K. Karami *et al.*, “Continuous and pulsed selective laser melting of Ti6Al4V lattice structures: Effect of post-processing on microstructural anisotropy and fatigue behaviour,” *Addit. Manuf.*, vol. 36, no. June, p. 101433, 2020, doi: 10.1016/j.addma.2020.101433.

[40] B. Zhang, Y. Li, and Q. Bai, “Defect Formation Mechanisms in Selective Laser Melting: A Review,” *Chinese J. Mech. Eng. (English Ed.*, vol. 30, no. 3, pp. 515–527, 2017, doi: 10.1007/s10033-017-0121-5.

[41] U. Scipioni, A. J. Wolfer, M. J. Matthews, J. R. Delplanque, and J. M. Schoenung, “On the limitations of Volumetric Energy Density as a design parameter for Selective Laser Melting,” *JMADE*, vol. 113, pp. 331–340, 2017, doi: 10.1016/j.matdes.2016.10.037.

[42] A. Poudel, M. S. Yasin, J. Ye, and J. Liu, “Feature-based volumetric defect classi fi ca-

tion in metal additive manufacturing," no. May, pp. 1–12, 2022, doi: 10.1038/s41467-022-34122-x.

[43] M. Grasso and B. M. Colosimo, "Process defects and in situ monitoring methods in metal powder bed fusion: A review," *Meas. Sci. Technol.*, vol. 28, no. 4, 2017, doi: 10.1088/1361-6501/aa5c4f.

[44] A. K. Singla *et al.*, "Selective laser melting of Ti6Al4V alloy: Process parameters, defects and post-treatments," *J. Manuf. Process.*, vol. 64, no. November 2020, pp. 161–187, 2021, doi: 10.1016/j.jmapro.2021.01.009.

[45] L. Zhang, Y. Liu, S. Li, and Y. Hao, "Additive Manufacturing of Titanium Alloys by Electron Beam Melting : A Review," vol. 1700842, pp. 1–16, 2018, doi: 10.1002/adem.201700842.

[46] J. Hao, W. Leong, E. Wong, and K. William, "An overview of powder granulometry on feedstock and part performance in the selective laser melting process," *Addit. Manuf.*, vol. 18, pp. 228–255, 2017, doi: 10.1016/j.addma.2017.10.011.

[47] G. Wegmann, R. Gerling, and F. P. Schimansky, "Temperature induced porosity in hot isostatically pressed gamma titanium aluminide alloy powders," *Acta Mater.*, vol. 51, no. 3, pp. 741–752, 2003, doi: 10.1016/S1359-6454(02)00465-2.

[48] A. Traff, "New developments in Hot Isostatic Press (HIP) Units," *Met. Powder Rep.*, vol. 45, no. 4, pp. 279–282, 1990, doi: 10.1016/S0026-0657(10)80055-4.

[49] H. V. Atkinson and S. Davies, "Fundamental aspects of hot isostatic pressing: An overview," *Metall. Mater. Trans. A Phys. Metall. Mater. Sci.*, vol. 31, no. 12, pp. 2981–3000, 2000, doi: 10.1007/s11661-000-0078-2.

[50] W. Zhou, K. Tsunoda, N. Nomura, and K. Yoshimi, "Effect of hot isostatic pressing on the microstructure and fracture toughness of laser additive-manufactured MoSiBTiC multiphase alloy," *Mater. Des.*, vol. 196, p. 109132, 2020, doi: 10.1016/j.matdes.2020.109132.

[51] M. H. Bocanegra-Bernal, "Hot Isostatic Pressing ( HIP ) technology and its," *J. Mater. Sci.*, vol. 9, pp. 6399–6420, 2004.

[52] J. Joseph, P. Hodgson, T. Jarvis, X. Wu, N. Stanford, and D. M. Fabijanic, "Effect of hot isostatic pressing on the microstructure and mechanical properties of additive manufactured AlxCoCrFeNi high entropy alloys," *Mater. Sci. Eng. A*, vol. 733, no. July, pp. 59–70, 2018, doi: 10.1016/j.msea.2018.07.036.

[53] E. Bassini *et al.*, "Study of the effects of aging treatment on astroloy processed via hot isostatic pressing," *Materials (Basel).*, vol. 12, no. 9, 2019, doi: 10.3390/ma12091517.

[54] C. Martínez *et al.*, "Effect of hot pressing and hot isostatic pressing on the microstructure, hardness, and wear behavior of nickel," *Mater. Lett.*, vol. 273, 2020, doi: 10.1016/j.matlet.2020.127944.

[55] S. Benito, J. Boes, M. Matsuo, S. Weber, and W. Theisen, "Uncovering process-structure relationships associated to the hot isostatic pressing of the high-speed steel

PMHS 3-3-4 through novel microstructural characterization methods," *Mater. Des.*, vol. 208, p. 109925, 2021, doi: 10.1016/j.matdes.2021.109925.

[56] V. Samarov, D. Seliverstov, and F. H. Froes, *Fabrication of near-net-shape cost-effective titanium components by use of prealloyed powders and hot isostatic pressing*. Elsevier Inc., 2015.

[57] A. Du Plessis *et al.*, "Metal Fabrication by Additive Manufacturing Using Laser and Electron Beam Melting Technologies," *Intermetallics*, vol. 28, no. 1, pp. 1–14, 2016, doi: 10.1016/S1005-0302(12)60016-4.

[58] H. zhong LI *et al.*, "Microstructure and high-temperature mechanical properties of near net shaped Ti−45Al−7Nb−0.3W alloy by hot isostatic pressing process," *Trans. Nonferrous Met. Soc. China (English Ed.*, vol. 30, no. 11, pp. 3006–3015, 2020, doi: 10.1016/S1003-6326(20)65438-3.

[59] C. H. Tam, S. C. Lee, and S. H. Chang, "The influence of canning HIP treatment on the microstructure characters of Cr35-Si65 and Cr50-Si50 targets," *Mater. Trans.*, vol. 50, no. 4, pp. 885–890, 2009, doi: 10.2320/matertrans.MER2008362.

[60] N. Perevoshchikova, C. R. Hutchinson, and X. Wu, "The design of hot-isostatic pressing schemes for Ti-5Al-5Mo-5V-3Cr (Ti-5553)," *Mater. Sci. Eng. A*, vol. 657, pp. 371–382, 2016, doi: 10.1016/j.msea.2016.01.082.

[61] A. I. Dekhtyar, V. I. Bondarchuk, V. V. Nevdacha, and A. V. Kotko, "The effect of microstructure on porosity healing mechanism of powder near-β titanium alloys under hot isostatic pressing in α + β-region: Ti-10V-2Fe-3Al," *Mater. Charact.*, vol. 165, no. May, p. 110393, 2020, doi: 10.1016/j.matchar.2020.110393.

[62] C. Cai *et al.*, "Effect of hot isostatic pressing procedure on performance of Ti6Al4V: Surface qualities, microstructure and mechanical properties," *J. Alloys Compd.*, vol. 686, pp. 55–63, 2016, doi: 10.1016/j.jallcom.2016.05.280.

[63] X. Yan *et al.*, "Effect of hot isostatic pressing (HIP) treatment on the compressive properties of Ti6Al4V lattice structure fabricated by selective laser melting," *Mater. Lett.*, vol. 255, p. 126537, 2019, doi: 10.1016/j.matlet.2019.126537.

[64] T. Childerhouse *et al.*, "The influence of finish machining depth and hot isostatic pressing on defect distribution and fatigue behaviour of selective electron beam melted Ti-6Al-4V," *Int. J. Fatigue*, vol. 147, no. January, pp. 1–11, 2021, doi: 10.1016/j.ijfatigue.2021.106169.

[65] C. Chen *et al.*, "Effect of hot isostatic pressing (HIP) on microstructure and mechanical properties of Ti6Al4V alloy fabricated by cold spray additive manufacturing," *Addit. Manuf.*, vol. 27, no. March, pp. 595–605, 2019, doi: 10.1016/j.addma.2019.03.028.

[66] H. Dang *et al.*, "A critical review on additive manufacturing of Ti-6Al-4V alloy : microstructure and mechanical properties," *J. Mater. Res. Technol.*, vol. 18, pp. 4641–4661, 2022, doi: 10.1016/j.jmrt.2022.04.055.

[67] J. Li, C. Yuan, J. Guo, J. Hou, and L. Zhou, "Effect of hot isostatic pressing on

microstructure of cast gas-turbine vanes of K452 alloy," *Prog. Nat. Sci. Mater. Int.*, vol. 24, no. 6, pp. 631–636, 2014, doi: 10.1016/j.pnsc.2014.10.008.

[68] W. E. Voice, M. Henderson, E. F. J. Shelton, and X. Wu, "Gamma titanium aluminide, TNB," *Intermetallics*, vol. 13, no. 9, pp. 959–964, 2005, doi: 10.1016/j.intermet.2004.12.021.

[69] F. Appel, M. Oehring, and R. Wagner, "Novel design concepts for gamma-base titanium aluminide alloys," *Intermetallics*, vol. 8, no. 9–11, pp. 1283–1312, 2000, doi: 10.1016/S0966-9795(00)00036-4.

[70] S. F. Franzén and J. Karlsson, "γ-Titanium Aluminide Manufactured by Electron Beam Melting," *Diploma Work No.37/2010, Master Program. Adv. Eng. Mater.*, p. 81, 2010.

[71] R. Biswas, A. S. Kuar, and S. Mitra, "Multi-objective optimization of hole characteristics during pulsed Nd:YAG laser microdrilling of gamma-titanium aluminide alloy sheet," *Opt. Lasers Eng.*, vol. 60, pp. 1–11, 2014, doi: 10.1016/j.optlaseng.2014.03.014.

[72] H. Zhu *et al.*, "Assessment of Titanium aluminide alloys for high-temperature nuclear structural applications," *Jom*, vol. 64, no. 12, pp. 1418–1424, 2012, doi: 10.1007/s11837-012-0471-5.

[73] P. Nov and F. Pr, "High-temperature oxidation of Ti e Al e Si alloys prepared by powder metallurgy u," vol. 810, 2019, doi: 10.1016/j.jallcom.2019.151895.

[74] E. A. Loria, "Quo vadis gamma titanium aluminide," *Intermetallics*, vol. 9, no. 12, pp. 997–1001, 2001, doi: 10.1016/S0966-9795(01)00064-4.

[75] R. A. Slepetys, P. A. Vaughan, and P. A. Vaughan, "Solid Solution of Aluminum Oxide in Rutile Titanium Dioxide1," vol. 78, no. 7, 1989.

[76] S. Biamino *et al.*, "Electron beam melting of Ti-48Al-2Cr-2Nb alloy: Microstructure and mechanical properties investigation," *Intermetallics*, vol. 19, no. 6, pp. 776–781, 2011, doi: 10.1016/j.intermet.2010.11.017.

[77] G. Baudana *et al.*, "Titanium aluminides for aerospace and automotive applications processed by Electron Beam Melting: Contribution of Politecnico di Torino," *Met. Powder Rep.*, vol. 71, no. 3, pp. 193–199, 2016, doi: 10.1016/j.mprp.2016.02.058.

[78] T. C. Dzogbewu, "Additive manufacturing of TiAl-based alloys," vol. 35, 2020.

[79] X. Wu, "Review of alloy and process development of TiAl alloys," *Intermetallics*, vol. 14, no. 10–11, pp. 1114–1122, 2006, doi: 10.1016/j.intermet.2005.10.019.

[80] R. Klingvall Ek, L.-E. Rännar, M. Bäckstöm, and P. Carlsson, "The effect of EBM process parameters upon surface roughness," *Rapid Prototyp. J.*, vol. 22, no. 3, pp. 495–503, Jan. 2016, doi: 10.1108/RPJ-10-2013-0102.

[81] B. Albert and N. Cedex, "Version of Record: https://www.sciencedirect.com/science/article/pii/S0165032720326483," pp. 5–10.

[82] Q. Feng *et al.*, “Research Progress of Titanium Sponge Production: A Review,” *Metals (Basel).*, vol. 13, no. 2, 2023, doi: 10.3390/met13020408.

[83] O. Dolev, S. Osovski, and A. Shirizly, “Ti-6Al-4V hybrid structure mechanical properties—Wrought and additive manufactured powder-bed material,” *Addit. Manuf.*, vol. 37, no. September 2020, p. 101657, 2021, doi: 10.1016/j.addma.2020.101657.

[84] T. S. Tshephe, S. O. Akinwamide, E. Olevsky, and P. A. Olubambi, “Additive manufacturing of titanium-based alloys- A review of methods, properties, challenges, and prospects,” *Heliyon*, vol. 8, no. 3, p. e09041, 2022, doi: 10.1016/j.heliyon.2022.e09041.

[85] S. Sahoo, O. Licata, B. Mazumder, and S. Roy, “Novel insights on the near atomic scale spatial distributions of substitutional alloying and interstitial impurity elements in Ti-6Al-4V alloy,” *J. Alloys Compd.*, vol. 907, p. 164511, 2022, doi: 10.1016/j.jallcom.2022.164511.

[86] S. A. Etesami, B. Fotovvati, and E. Asadi, “Heat treatment of Ti-6Al-4V alloy manufactured by laser-based powder-bed fusion: Process, microstructures, and mechanical properties correlations,” *J. Alloys Compd.*, vol. 895, p. 162618, 2022, doi: 10.1016/j.jallcom.2021.162618.

[87] A. Zafari, M. R. Barati, and K. Xia, “Controlling martensitic decomposition during selective laser melting to achieve best ductility in high strength Ti-6Al-4V,” *Mater. Sci. Eng. A*, vol. 744, no. December 2018, pp. 445–455, 2019, doi: 10.1016/j.msea.2018.12.047.

[88] J. Chen, D. Fabijanic, T. Zhang, E. W. Lui, M. Brandt, and W. Xu, “Deciphering the transformation pathway in laser powder-bed fusion additive manufacturing of Ti-6Al-4V alloy,” *Addit. Manuf.*, vol. 58, no. July, 2022, doi: 10.1016/j.addma.2022.103041.

[89] W. Xu *et al.*, “Additive manufacturing of strong and ductile Ti-6Al-4V by selective laser melting via in situ martensite decomposition,” *Acta Mater.*, vol. 85, pp. 74–84, 2015, doi: 10.1016/j.actamat.2014.11.028.

[90] P. WANG *et al.*, *A review of particulate-reinforced aluminum matrix composites fabricated by selective laser melting*, vol. 30, no. 8. 2020.

[91] L. Thijs, F. Verhaeghe, T. Craeghs, J. Van Humbeeck, and J. P. Kruth, “A study of the microstructural evolution during selective laser melting of Ti-6Al-4V,” *Acta Mater.*, vol. 58, no. 9, pp. 3303–3312, 2010, doi: 10.1016/j.actamat.2010.02.004.

[92] “Arcam EBM A2X,” p. 2.

[93] A. I. All, A. Industries, A. Industries, A. W. Platform, and A. Industries, “No Title.”

[94] Y. Liu *et al.*, “Investigations on processing powder metallurgical high-Nb TiAl alloy sheets,” *Intermetallics*, vol. 55, pp. 80–89, 2014, doi: 10.1016/j.intermet.2014.07.013.

[95] R. Gao, H. Peng, H. Guo, and B. Chen, “A Combined Powder Metallurgical Approach to Process Gamma-TiAl with Composite Structure,” *Metall. Mater. Trans. A Phys. Metall. Mater. Sci.*, vol. 53, no. 7, pp. 2351–2368, 2022, doi: 10.1007/s11661-022-

06703-4.

[96] R. Wartbichler *et al.*, “On the Formation Mechanism of Banded Microstructures in Electron Beam Melted Ti–48Al–2Cr–2Nb and the Design of Heat Treatments as Remedial Action,” *Adv. Eng. Mater.*, vol. 23, no. 12, 2021, doi: 10.1002/adem.202101199.

[97] C. Ghibaudo, R. Wartbichler, G. Marchese, H. Clemens, D. Ugues, and S. Biamino, “Influence of focus offset on the microstructure of an intermetallic γ-TiAl based alloy produced by electron beam powder bed fusion,” *J. Manuf. Process.*, vol. 89, no. February, pp. 132–141, 2023, doi: 10.1016/j.jmapro.2023.01.061.

[98] J. Bieske, M. Franke, M. Schloffer, and C. Köerner, “Microstructure and properties of TiAl processed via an electron beam powder bed fusion capsule technology,” *Intermetallics*, vol. 126, no. May, 2020, doi: 10.1016/j.intermet.2020.106929.

[99] H. Bakhshi Farkoush, G. Marchese, E. Bassini, A. Aversa, and S. Biamino, “Microstructure of TiAl Capsules Processed by Electron Beam Powder Bed Fusion Followed by Post-Hot Isostatic Pressing,” *Materials (Basel).*, vol. 16, no. 16, 2023, doi: 10.3390/ma16165510.

[100] G. Li *et al.*, “The Effect of Hot Oscillatory Pressing Temperature on Microstructure and Tensile Behavior of Powder Metallurgy Superalloy,” *Metals (Basel).*, vol. 12, no. 10, 2022, doi: 10.3390/met12101652.

[101] L. Xu, R. Guo, C. Bai, J. Lei, and R. Yang, “Effect of Hot Isostatic Pressing Conditions and Cooling Rate on Microstructure and Properties of Ti-6Al-4V Alloy from Atomized Powder,” *J. Mater. Sci. Technol.*, vol. 30, no. 12, pp. 1289–1295, 2014, doi: 10.1016/j.jmst.2014.04.011.

[102] K. Zhang, J. Mei, N. Wain, and X. Wu, “Effect of hot-isostatic-pressing parameters on the microstructure and properties of powder Ti-6Al-4V hot-isostatically-pressed samples,” *Metall. Mater. Trans. A Phys. Metall. Mater. Sci.*, vol. 41, no. 4, pp. 1033–1045, 2010, doi: 10.1007/s11661-009-0149-y.

[103] H. P. Tang *et al.*, “Microstructure, Mechanical Properties, and Flatness of SEBM Ti-6Al-4V Sheet in As-Built and Hot Isostatically Pressed Conditions,” *Jom*, vol. 69, no. 3, pp. 466–471, 2017, doi: 10.1007/s11837-016-2253-y.

[104] T. Mishurova, S. Evsevleev, P. Piault, A. King, L. Henry, and G. Bruno, “Understanding the hot isostatic pressing effectiveness of laser powder bed fusion Ti-6Al-4V by in-situ X-ray imaging and diffraction experiments,” *Sci. Rep.*, vol. 13, no. 1, pp. 1–11, 2023, doi: 10.1038/s41598-023-45258-1.

[105] N. Eshawish, S. Malinov, W. Sha, and P. Walls, “Microstructure and Mechanical Properties of Ti-6Al-4V Manufactured by Selective Laser Melting after Stress Relieving, Hot Isostatic Pressing Treatment, and Post-Heat Treatment,” *J. Mater. Eng. Perform.*, vol. 30, no. 7, pp. 5290–5296, 2021, doi: 10.1007/s11665-021-05753-w.

[106] X. Yan *et al.*, “Effect of heat treatment on the phase transformation and mechanical properties of Ti6Al4V fabricated by selective laser melting,” *J. Alloys Compd.*, vol. 764,

pp. 1056–1071, 2018, doi: 10.1016/j.jallcom.2018.06.076.

[107] J. Besson and M. Abouaf, “Microstructural Changes in Alumina during {HIP},” *Mater. Sci. Engng A*, vol. 109A, pp. 37–43, 1989.

[108] A. Hattal *et al.*, “Effect of hot isostatic pressing on microstructure and mechanical properties of Ti6Al4V-zirconia nanocomposites processed by laser-powder bed fusion,” *Mater. Des.*, vol. 214, 2022, doi: 10.1016/j.matdes.2022.110392.

[109] A. Abu-Issa *et al.*, “Effects of altered hot isostatic pressing treatments on the microstructures and mechanical performance of electron beam melted Ti-6Al-4V,” *J. Mater. Res. Technol.*, vol. 9, no. 4, pp. 8735–8743, 2020, doi: 10.1016/j.jmrt.2020.06.019.

[110] J. Cho, “Characterization of the α’-Martensite phase and its decomposition in Ti-6Al-4V additively manufactured by selective laser melting,” p. 197, 2018.